The radial abundance gradient of oxygen towards the Galactic anti-centre

C. Esteban,[1,2]★ X. Fang,[3,4]★ J. García-Rojas[1,2]★ and L. Toribio San Cipriano[1,2]

[1]*Instituto de Astrofísica de Canarias, E-38200 La Laguna, Tenerife, Spain*
[2]*Departamento de Astrofísica, Universidad de La Laguna, E-38206 La Laguna, Tenerife, Spain*
[3]*Laboratory for Space Research, Faculty of Science, University of Hong Kong, Pokfulam Road, Hong Kong 0000-0002-6536-5575, China*
[4]*Department of Earth Sciences, Faculty of Science, University of Hong Kong, Pokfulam Road, Hong Kong 0000-0002-6536-5575, China*

ABSTRACT

We present deep optical spectroscopy of eight H II regions located in the anti-centre of the Milky Way. The spectra were obtained at the 10.4 m GTC and 8.2 m VLT. We determined T_e([N II]) for all objects and T_e([O III]) for six of them. We also included in our analysis an additional sample of 13 inner-disc Galactic H II regions from the literature that have excellent T_e determinations. We adopted the same methodology and atomic data set to determine the physical conditions and ionic abundances for both samples. We also detected the C II and O II optical recombination lines in Sh 2-100, which enables the determination of the abundance discrepancy factor for this object. We found that the slopes of the radial oxygen gradients defined by the H II regions from R_{25} (=11.5 kpc) to 17 kpc and those within R_{25} are similar within the uncertainties, indicating the absence of flattening in the radial oxygen gradient in the outer Milky Way. In general, we found that the scatter of the O/H ratios of H II regions is not substantially larger than the observational uncertainties. The largest possible local inhomogeneities of the oxygen abundances are of the order of 0.1 dex. We also found positive radial gradients in T_e([O III]) and T_e([N II]) across the Galactic disc. The shapes of these temperature gradients are similar and also consistent with the absence of flattening of the metallicity distribution in the outer Galactic disc.

Key words: ISM: abundances – H II regions – Galaxy: abundances – Galaxy: disc – Galaxy: evolution.

1 INTRODUCTION

The spatial distributions of abundances of chemical elements across galactic discs – the radial gradients – have been derived for many galaxies and are key to understanding the chemical evolution of galaxies. These gradients reflect the star formation history as well as the effects of gas flows in stellar systems. H II regions are fundamental probes to trace the present-day composition of the gas-phase interstellar medium. They have been widely used to determine the radial abundance gradients – especially for O, a proxy of metallicity in the analysis of ionized gaseous nebula – in the Milky Way and other spiral galaxies. Some authors have claimed – based on both the H II region and planetary nebula data – that radial abundance gradients may flatten at the outer parts of the Milky Way disc (e.g. Fich & Silkey 1991; Vílchez & Esteban 1996; Maciel, Lago & Costa 2006), although other authors do not support such claims (e.g. Caplan et al. 2000; Henry et al. 2010). Metallicity determinations of other kinds of objects, such as cepheids (e.g. Luck et al. 2003; Pedicelli et al. 2009; Lemasle et al. 2013) and Galactic

open clusters (e.g. Yong, Carney & Friel 2012), find in general some hints of such flattening but some of them do not.

There is strong evidence for flat radial gradients from the spectroscopic observations of H II regions in the outer discs of some nearby spiral galaxies, as in the cases of M83, NGC 1512 or NGC 3621 (Bresolin et al. 2009; Bresolin, Kennicutt & Ryan-Weber 2012) among others. Moreover, Sánchez et al. (2014) presented a catalogue of H II regions in several hundred galaxies from the CALIFA survey and many of them show an external flattening in oxygen. Flattening or even the upturn of the metallicity gradient has also been found from photometry of red giant branch stars in the outer discs of spiral galaxies NGC 300 and NGC 7793 (e.g. Vlajić, Bland-Hawthorn & Freeman 2011). Bresolin et al. (2012) and more recently Bresolin (2016) discuss several mechanisms that can produce such flattening: leveling of the star formation efficiency, stellar migration, radial metal mixing or enriched gas infall. These authors indicate that the flattening of the radial abundance gradients in external spiral galaxies occurs approximately at the isophotal radius, R_{25}, which in the case of the Milky Way is about 11.5 kpc (de Vaucouleurs & Pence 1978). Metallicity studies based on Galactic cepheids and open clusters indicate that the change in the slope of the Milky Way occurs at about 9 kpc (Lépine et al. 2011). Esteban et al. (2013) obtained very deep spectra of the bright H II

★ E-mail: cel@iac.es (CE); fangx@hku.hk (XF); jogarcia@iac.es (JGR)

region NGC 2579, which is located at a Galactocentric distance of 12.4 kpc, close to R_{25}, the best data ever taken for an H II region at the outer Galactic disc. They found that their O/H and C/H ratios are consistent with flattened gradients. Very recently, Fernández-Martín et al. (2017) presented the 4.2 m *WHT* spectroscopic observations of nine H II regions located at $R_G > 11$ kpc, but only detected the temperature-sensitive auroral lines in five of them. In addition, these authors re-analysed the data of other H II regions retrieved from the literature. The results of Fernández-Martín et al. (2017) do not confirm the presence of flattening at the Galactic anti-centre, and they point out the necessity of more observations of H II regions in the outer part of the Galaxy to establish the true shape of the metallicity gradient.

The paucity of accurate abundance determinations for H II regions in the anti-centre direction has been an enduring problem in the exploration of the shape of the O gradient in the Galactic disc. Those distant nebulae are usually faint and the number of such cases with direct determinations of electron temperature, T_e, is rather limited. A high-quality determination of T_e is essential to obtain reliable O abundances. We have carried out a project to obtain very deep spectroscopy of a selected sample of H II regions located close to or beyond R_{25} in order to increase the sample with reliable measurements of the O/H ratios in the direction of Galactic anti-centre. We have selected a sample of eight relatively bright objects with R_G in the range 9.4–17.0 kpc that shows a high ionization degree, $I($O III$] \lambda5007)/I($H $\beta) \geq 1.0$, for ensuring as much as possible the detection of the [O III] $\lambda4363$ auroral line. These sample is complemented with some other outer-disc H II regions, NGC 2579 (Esteban et al. 2013), Sh 2-311 (García-Rojas et al. 2005) and NGC 7635 (Esteban et al. 2016b), which were previously observed and published by our group and for which we have excellent determinations of T_e.

2 OBSERVATIONS AND DATA REDUCTION

2.1 Observations

Except Sh 2-298, observations of all objects were performed with the 10.4 m Gran Telescopio Canarias (GTC) at Observatorio del Roque de los Muchachos (ORM, La Palma, Spain). They were carried out in fourteen 1 h observing blocks distributed in several nights between September and November in 2015. The spectra were obtained with the OSIRIS (Optical System for Imaging and low-Intermediate-Resolution Integrated Spectroscopy) spectrograph (Cepa et al. 2000, 2003). OSIRIS consists of a mosaic of two Marconi CCD42-82 CCDs (CCD1+CCD2), each with 2048 × 4096 pixels, and a 74-pixel gap between them. Each pixel has a physical size of 15 μm. The standard readout mode of 2 × 2 pixel binning was adopted during observations, which gives a plate scale of 0.254 arcsec. The long-slit spectroscopy mode was used in our OSIRIS observations and all targets were located at the centre of CCD2. The slit length was 7.4 arcmin and its width was set at 0.8 arcsec, same as the typical seeing at ORM. Two OSIRIS grisms, R1000B and R2500V, were used for the spectroscopy. R1000B covers almost the whole optical wavelength range, from 3600 to 7750 Å, while R2500V covers from 4430 to 6020 Å but with higher spectral resolution for the wavelength region where the T_e-sensitive [O III] $\lambda4363$ line lies. The effective spectral resolution (full width at half-maximum, FWHM) was 6.52 Å for the R1000B grism and 2.46 Å for R2500V. The long slit covers the brightest regions of the nebulae. Coordinates of the slit centre and the position angle (PA) of the long-slit are given in Table 1, where we also present

the integration time of each object. In the two-dimensional (2D) spectrum of each object, we selected the brightest region along the slit to extract the highest signal-to-noise 1D spectrum. In Figs 1 and 2, we mark the slit position and aperture of spectral extraction for each object. The aperture size of extraction along the slit is indicated in the seventh column of Table 1. The OSIRIS spectra were wavelength calibrated using the HgAr, Ne and Xe arc lamps.

The observations of Sh 2-298 were made on 2003 November 14 and December 2 with the Ultraviolet Visual Echelle Spectrograph (UVES; D'Odorico et al. 2000), on the Very Large Telescope (VLT) Kueyen unit at Cerro Paranal Observatory (Chile). The adopted standard settings in both the red and blue arms of the spectrograph cover a broad region from 3100 to 10 400 Å. The wavelength intervals 5783–5830 and 8540–8650 Å were not observed due to a gap between the two CCDs used in the red arm. There are also five narrow gaps that were not observed, 9608–9612, 9761–9767, 9918–9927, 10 080–10 093 and 10 249–10 264 Å, because the five redmost orders did not fit completely within the CCD. The atmospheric dispersion corrector (ADC) was used to keep the same observed region within the slit regardless of the air mass value. The slit width was set to 3 arcsec and the slit length to 8 arcsec. The effective resolution at a given wavelength is approximately $\Delta\lambda \sim \lambda/8800$. Spectroscopic observations of the spectrophotometric standard star HD 49798 (Turnshek et al. 1990; Bohlin & Lindler 1992) were made for the flux calibration.

2.2 Data reduction

The GTC OSIRIS long-slit spectra were reduced using IRAF[1] v2.16. Data reduction followed the standard procedure for long-slit spectra. We first removed cosmic rays by combining the raw spectrograms of each H II region and then subtracted the bias and corrected for the flat-field. We then carried out wavelength calibration using the arc-line spectra. According to the coverage of arc lines across the wavelength range of the grism, we used the HgAr arc lines for the calibration of the R1000B spectra and HgAr+Ne+Xe for the R2500V spectra. The geometry distortion of emission lines along the long slit exists for extended sources. During the wavelength calibration, this geometry distortion was also rectified by fitting the arc lines with sixth- or seventh-order polynomial functions in the 2D spectrogram. We then applied the resolution derived from fitting of the arc-line spectrogram to the target spectrum. Through this procedure, all nebular emission lines (also the sky emission lines) in a 2D spectrum were 'straightened' along the long slit.

Particular care was taken in the background subtraction because the sky background emission is inhomogeneous along the GTC OSIRIS long slit (Fang et al. 2015). The emission profiles of the sky background along the slit direction were first fitted with polynomial functions and then subtracted from the spectrogram. Since our targets are all extended sources, low-order polynomial functions were adopted for the profile fitting so that the true nebular emission was not removed due to a possible over-subtraction. The BACKGROUND package in IRAF was used in the background subtraction. This procedure produced a cleaned spectrogram for each target, which was then flux-calibrated (and also corrected for the atmospheric extinction) using the spectrum of a spectrophotometric standard star.

---

[1] IRAF, the Image Reduction and Analysis Facility, is distributed by the National Optical Astronomy Observatory, which is operated by the Association of Universities for Research in Astronomy under cooperative agreement with the National Science Foundation.

Table 1. Journal of observations.

H II region	R.A.[a] (J2000)	Decl.[a] (J2000)	R_G^b (kpc)	Telescope/ /Spectrograph	PA (°)	Extracted area (arcsec^2)	Grating or configuration	Exposure time (s)
Sh 2-83	19:24:52.55	+20:47:24.4	15.3 ± 0.1	GTC/OSIRIS	90	38.1 × 0.8	R1000B	3 × 882
							R2500V	3 × 882
Sh 2-100	20:02:00.69	+33:29:23.9	9.4 ± 0.3	GTC/OSIRIS	−55	28.5 × 0.8	R1000B	3 × 882
							R2500V	3 × 882
Sh 2-127	21:28:40.95	+54:42:13.9	14.2 ± 1.0	GTC/OSIRIS	1	6.9 × 0.8	R1000B	3 × 882
							R2500V	3 × 882
Sh 2-128	21:32:49.86	+55:53:16.2	12.5 ± 0.4	GTC/OSIRIS	86	24.1 × 0.8	R1000B	3 × 882
							R2500V	3 × 882
Sh 2-209	04:11:25.69	+51:14:33.8	17.0 ± 0.7	GTC/OSIRIS	35	45.7 × 0.8	R1000B	3 × 882
							R2500V	3 × 882
Sh 2-212	04:40:56.13	+50:26:53.1	14.6 ± 1.4	GTC/OSIRIS	−70	38.1 × 0.8	R1000B	3 × 882
							R2500V	3 × 882
Sh 2-288	07:08:48.90	+07:08:48.9	14.1 ± 0.4	GTC/OSIRIS	−32	28.5 × 0.8	R1000B	3 × 882
							R2500V	3 × 882
Sh 2-298	07:18:28.10	−13:17:19.7	11.9 ± 0.7	VLT/UVES	90	8 × 3	DIC1(346+580)	3 × 540
							DIC2(437+860)	3 × 1620

Notes. [a]Coordinates of the slit centre.
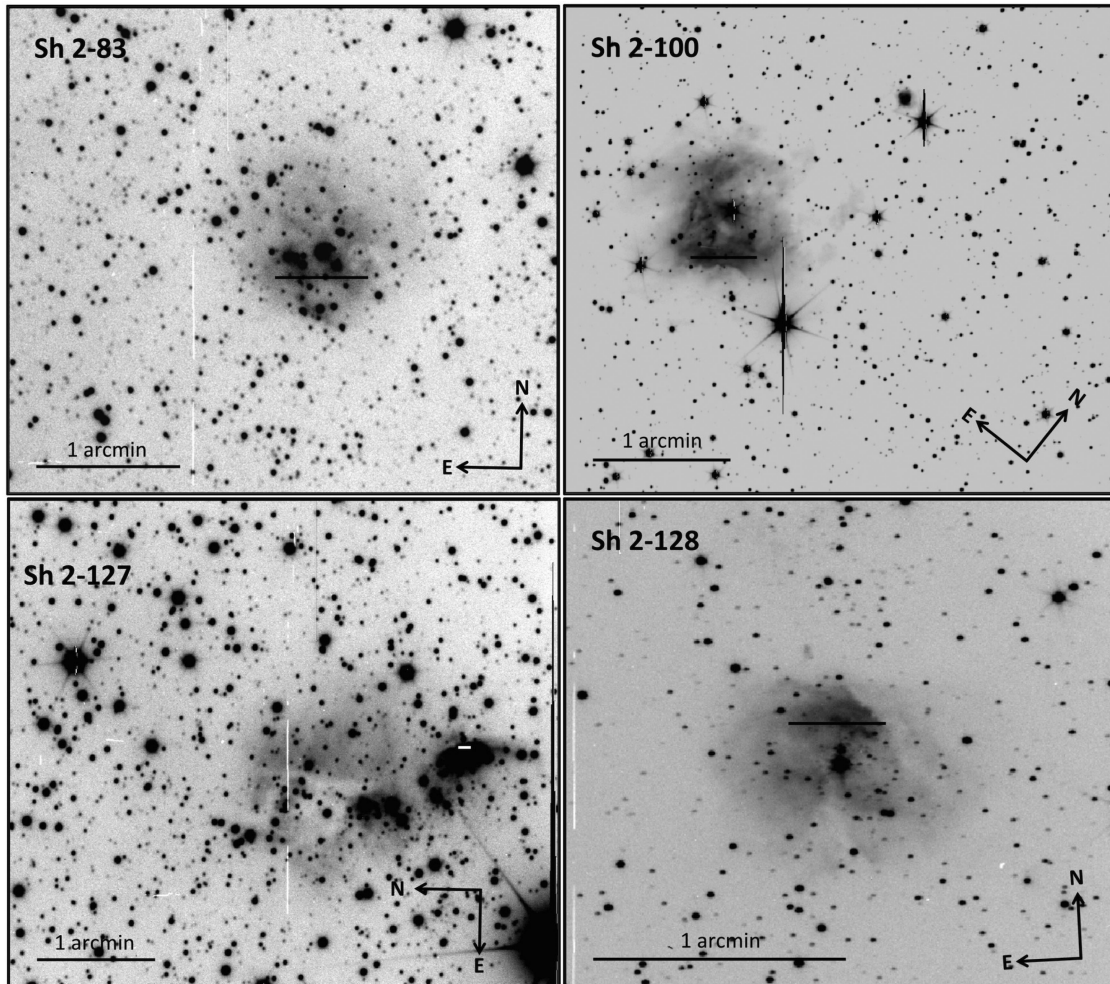[b]Galactocentric distances assuming the Sun at 8 kpc.

Figure 1. The GTC *g*-band acquisition images of Sh 2-83, Sh 2-100, Sh 2-127 and Sh 2-128. The position and length of the aperture extracted for each object are indicated.
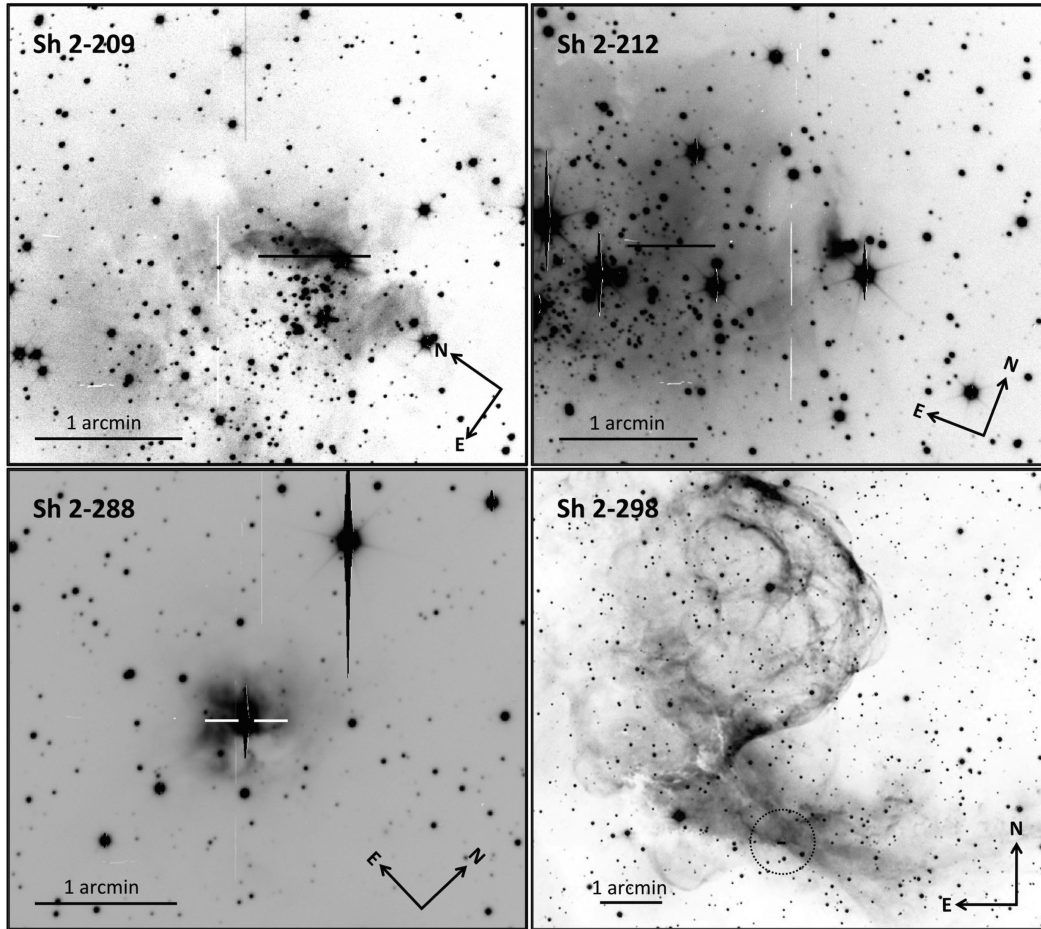
Figure 2. The GTC *g*-band acquisition images of Sh 2-209, Sh 2-212 and Sh 2-288. The image of Sh 2-298 is a combination of the *B*, *V* and Hα images obtained with the Wide Field Camera at the 2.5m INT (ORM) by Á. R. López-Sánchez (AAO, CSIRO, Australia). The position and length of the aperture extracted for each object are indicated.

Finally, we extracted 1D spectrum from the cleaned, fully calibrated 2D frame for each H II region, using the slit aperture indicated in Figs 1 and 2. As an example, Fig. 3 shows the extracted 1D spectra for Sh 2-100. The temperature-sensitive [O III] $\lambda4363$ and [N II] $\lambda5755$ auroral lines are well detected. In the sections below, we will also analyse the optical recombination lines of C II and O II that were also observed in the deep spectra of this target. It is worth mentioning that the second-order contamination exists in the red part (>6300 Å) of the OSIRIS R1000B grism. We corrected for this effect by fitting the overall shape of the derived R1000B efficiency curve with a fifth-order polynomial function. This correction has proved to be reliable (Fang et al. 2015).

The VLT UVES echelle spectra of Sh 2-298 were reduced using the ECHELLE reduction package in IRAF, following the standard procedure of bias subtraction, aperture extraction, flat-fielding, wavelength calibration and then flux calibration.

3 LINE INTENSITY MEASUREMENTS

Emission line fluxes of the spectra of the eight H II regions included in Table 1 were measured with the SPLOT routine of IRAF by integrating over the emission line profile between two given limits and over the average local continuum. All line fluxes of a given spectrum have been normalized to H$\beta = 100$. In the wavelength range between 4430 and 6020 Å of the GTC spectra, the emis-

sion line fluxes measured from the R2500V spectrum were used instead of those measured from the R1000B spectrum, although our flux calibration was reliable and the spectral-line measurements obtained with the two OSIRIS grisms agree well with each other. The S/Ns of faint emission lines are higher in the spectra taken with the grism R2500V. In the case of line blending, we applied double- or multiple-Gaussian profile fit using the SPLOT routine of IRAF to measure the individual line intensities. Identification of emission lines were made following our previous works on the spectroscopy of bright Galactic H II regions (see García-Rojas & Esteban 2007, and references therein).

The logarithmic reddening coefficient, $c(H\beta)$, was derived by comparing the observed flux ratios of the brightest H I Balmer lines (Hα, Hγ and Hδ) with the Case B theoretical calculations of Storey & Hummer (1995). The theoretical ratios of the H I lines were calculated for the nebular physical conditions diagnosed for each H II region, and T_e and N_e were determined following an iterative process (see Section 6.1 for details). We have used the reddening function, $f(\lambda)$, normalized to Hβ derived by Cardelli, Clayton & Mathis (1989) and assumed $R_V = 3.1$.

In Tables 2–4, we present emission line measurements of the eight H II regions: the emission line identifications are given in the first three columns; the reddening function, $f(\lambda)$, is in the fourth column; the dereddened and normalized (with respect to H$\beta = 100$) line intensities are presented in the rest columns. The quoted
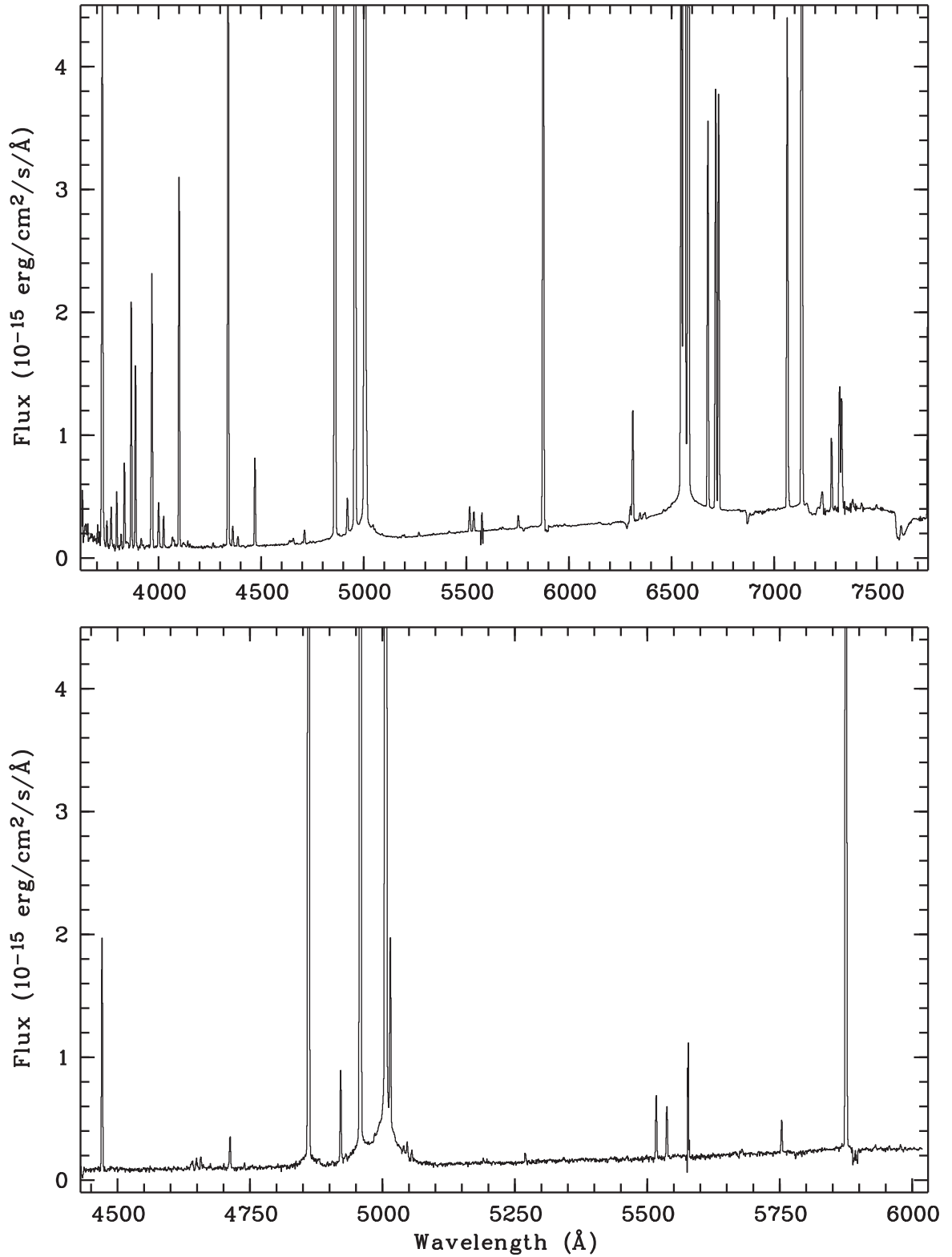
Figure 3. The GTC OSIRIS long-slit 1D spectra of Sh 2-100 obtained with the R1000B (top panel) and R2500V (bottom panel) grisms. Spectra have been fully calibrated, but the interstellar extinction has not been corrected for.

line intensity errors include the uncertainties in the flux measurements and the error propagation of the reddening coefficient. The reddening coefficient $c(H\beta)$ and the observed $H\beta$ line flux $F(H\beta)$, as measured from the extracted 1D spectrum, of each H II region are

presented in the final two rows of each table. In the case of Sh 2-298 (Table 4), we give two decimals for the laboratory wavelength of the lines because of the much higher spectral resolution of the VLT UVES observations.

Table 2. Derredened line intensity ratios with respect to $I(H\beta) = 100$ for Sh 2-100, Sh 2-128, Sh 2-288 and Sh 2-127.

λ_0 (Å)	Ion	ID	$f(\lambda)$	Sh 2-100	Sh 2-128	Sh 2-288	Sh 2-127
					$I(\lambda)/I(H\beta)$		
3704	H I	H16	0.260	0.99 ± 0.22	–	–	–
3705	He I	25					
3712	H I	H15	0.259	0.67 ± 0.23	–	–	–
3726	[O II]	1F	0.257	68.0 ± 4.4	217.5 ± 6.9	317 ± 22	366 ± 11
3729	[O II]	1F					
3750	H I	H12	0.253	2.25 ± 0.26	–	3.21 ± 0.45	8.2:
3771	H I	H11	0.249	3.36 ± 0.44	–	2.92 ± 0.41	–
3798	H I	H10	0.244	4.53 ± 0.44	5.5 ± 2.0	3.73 ± 0.68	–
3820	He I	22	0.240	1.02 ± 0.17	–	–	–
3835	H I	H9	0.237	7.00 ± 0.53	7.9 ± 1.5	6.31 ± 0.69	10.2 ± 2.5
3867	He I	20	0.231	20.6 ± 1.3	9.8 ± 1.8	–	–
3869	[Ne III]	1F					
3889	He I	5	0.227	14.93 ± 0.90	17.1 ± 1.4	16.3 ± 1.2	20.4 ± 2.9
3889	H I	H8					
3967	[Ne III]	1F	0.211	23.3 ± 1.3	20.3 ± 1.3	–	–
3970	H I	H7				15.7 ± 1.1	–
4026	He I	18	0.198	2.22 ± 0.17	–	1.68 ± 0.18	–
4069	[S II]	1F	0.189	0.727 ± 0.051	–	1.40 ± 0.18	–
4076	[S II]	1F	0.187	0.339 ± 0.024	–	0.37 ± 0.14	–
4102	H I	H6	0.182	25.96 ± 1.23	26.2 ± 1.2	26.1 ± 1.3	26.1 ± 1.3
4144	He I	53	0.172	0.293 ± 0.069	–	–	–
4156	N II	19	0.171	0.125 ± 0.043	–	–	–
4267	C II	6	0.144	0.249 ± 0.049	–	–	–
4340	H I	Hγ	0.127	44.44 ± 1.60	45.0 ± 1.0	44.4 ± 1.7	44.8 ± 1.1
4363	[O III]	2F	0.121	1.145 ± 0.065	1.76 ± 0.18	0.58 ± 0.11	–
4388	He I	51	0.115	0.529 ± 0.046	–	–	–
4471	He I	14	0.096	4.85 ± 0.15	4.18 ± 0.23	3.00 ± 0.15	2.77 ± 0.25
4607	[Fe III]	3F	0.062	–	–	0.076 ± 0.020	–
4639	O II	1	0.055	0.217 ± 0.038	–	0.062 ± 0.023	–
4642	O II	1					
4643	N II	5					
4649	O II	1	0.052	0.183 ± 0.029	–	–	–
4651	O II	1					
4658	[Fe III]	3F	0.050	0.213 ± 0.019	0.300 ± 0.046	1.086 ± 0.045	0.645 ± 0.052
4662	O II	1	0.049	0.041 ± 0.008	–	–	–
4676	O II	1	0.043	0.036 ± 0.009	–	–	–
4702	[Fe III]	3F	0.039	0.072 ± 0.011	–	0.262 ± 0.039	–
4711	[Ar IV]	1F	0.037	0.598 ± 0.035	0.516 ± 0.065	0.303 ± 0.029	0.500 ± 0.082
4713	He I	12	0.036				
4734	[Fe III]	3F	0.031	–	–	0.075 ± 0.013	–
4740	[Ar IV]	1F	0.030	0.090 ± 0.019	–	–	–
4755	[Fe III]	3F	0.026	–	–	0.198 ± 0.014	–
4770	[Fe III]	3F	0.023	–	–	0.049 ± 0.007	–
4778	[Fe III]	3F	0.021	–	–	0.017 ± 0.008	–
4789	[Fe III]		0.018	–	–	0.044 ± 0.015	–
4815	[Fe II]	20F	0.012	–	–	0.085 ± 0.018	–
4861	H I	Hβ	0.000	100.0 ± 2.0	100.0 ± 2.0	100.0 ± 2.0	100.0 ± 2.0
4881	[Fe III]	2F	−0.005	–	–	0.237 ± 0.029	0.222 ± 0.051
4922	He I	48	−0.015	1.323 ± 0.074	1.200 ± 0.088	0.738 ± 0.041	0.855 ± 0.051
4959	[O III]	1F	−0.024	126.9 ± 2.6	90.6 ± 1.8	41.09 ± 0.87	20.02 ± 0.41
4987	[Fe III]	2F	−0.031	–	0.192 ± 0.039	0.274 ± 0.022	–
5007	[O III]	1F	−0.036	341.9 ± 7.4	271.0 ± 5.5	117.0 ± 2.6	58.7 ± 1.2
5016	He I	4	−0.038	2.34 ± 0.30	2.386 ± 0.072	1.795 ± 0.061	1.864 ± 0.060
5035	[Fe II]	4F	−0.043	–	–	0.031 ± 0.002	–
5048	He I	47	−0.046	0.179 ± 0.029	0.265 ± 0.048	0.109 ± 0.024	–
5056	Si II	5	−0.048	0.120 ± 0.010	0.144 ± 0.028	0.215 ± 0.020	–
5159	[Fe II]	19F	−0.073	–	–	0.067 ± 0.015	–
5192	[Ar III]	3F	−0.081	0.043 ± 0.007	–	–	–
5198	N I	1F	−0.082	0.015 ± 0.002	0.183 ± 0.032	0.763 ± 0.033	0.123 ± 0.031
5200	N I	1F	−0.083	–	–	–	0.055:
5262	[Fe II]	19F	−0.098	–	–	0.072 ± 0.007	–
5270	[Fe III]	1F	−0.111	0.099 ± 0.012	0.262 ± 0.022	0.518 ± 0.027	0.414 ± 0.036
5518	[Cl III]	1F	−0.154	0.523 ± 0.025	0.532 ± 0.035	0.405 ± 0.022	0.423 ± 0.046

Table 2 – *continued*

λ_0 (Å)	Ion	ID	f(λ)	Sh 2-100	Sh 2-128	Sh 2-288	Sh 2-127
					$I(\lambda)/I(H\beta)$		
5538	[Cl III]	1F	−0.158	0.422 ± 0.024	0.426 ± 0.028	0.305 ± 0.019	0.393 ± 0.056
5755	[N II]	3F	−0.194	0.188 ± 0.013	0.616 ± 0.028	0.864 ± 0.047	1.290 ± 0.043
5876	He I	11	−0.215	15.65 ± 0.85	13.01 ± 0.33	8.78 ± 0.51	9.51 ± 0.25
5958	O I	23	−0.228	–	–	0.074 ± 0.014	–
5979	Si II	4	−0.231	–	–	0.093 ± 0.008	–
6046	O I	22	−0.242	–	–	0.068 ± 0.012	–
6300	[O I]	1F	−0.282	0.157 ± 0.026	0.833 ± 0.041	1.10 ± 0.11	–
6312	[S III]	3F	−0.283	1.44 ± 0.11	1.456 ± 0.060	1.29 ± 0.11	1.83 ± 0.13
6347	Si II	4	−0.289	0.082 ± 0.017	0.040 ± 0.010	0.139 ± 0.026	0.116 ± 0.025
6364	O I	1F	−0.291	0.047 ± 0.012	0.278 ± 0.031	0.493 ± 0.082	–
6371	Si II	2	−0.292	0.080 ± 0.019	–	–	–
6548	[N II]	1F	−0.318	5.77 ± 0.45	11.21 ± 0.33	21.6 ± 1.8	30.01 ± 0.89
6563	H I	Hα	−0.320	100.1 ± 7.8[a]	288.7 ± 8.6	183 ± 15[a]	289.1 ± 8.6
6583	[N II]	1F	−0.323	19.5 ± 1.5	36.8 ± 1.1	68.0 ± 5.7	90.1 ± 2.7
6678	He I	46	−0.336	4.11 ± 0.33	3.49 ± 0.12	2.20 ± 0.20	2.454 ± 0.083
6716	[S II]	2F	−0.342	4.19 ± 0.35	8.66 ± 0.27	13.4 ± 1.2	13.38 ± 0.41
6731	[S II]	2F	−0.344	4.09 ± 0.34	8.52 ± 0.27	13.0 ± 1.2	14.09 ± 0.44
7002	O I	21	−0.379	–	–	0.058 ± 0.012	–
7065	He I	10	−0.387	4.39 ± 0.41	2.98 ± 0.10	3.22 ± 0.32	2.478 ± 0.086
7136	[Ar III]	1F	−0.396	13.7 ± 1.3	10.77 ± 0.37	5.79 ± 0.59	6.48 ± 0.22
7155	[Fe II]	14F	−0.399	–	–	0.036 ± 0.010	–
7236	C II	3	−0.408	–	–	0.098 ± 0.021	–
7281	He I	45	−0.414	0.554 ± 0.059	0.540 ± 0.036	0.353 ± 0.066	0.278 ± 0.045
7318	[O II]	2F	−0.418	0.82 ± 0.10	2.71 ± 0.10	3.92 ± 0.43	4.67 ± 0.33
7320	[O II]	2F					
7330	[O II]	2F	−0.420	0.735 ± 0.092	2.480 ± 0.093	3.38 ± 0.37	4.63 ± 0.32
7331	[O II]	2F					
7751	[Ar III]	2F	−0.467	–	1.284 ± 0.059	–	0.762 ± 0.080
c(Hβ)				1.73 ± 0.10	2.27 ± 0.03	1.34 ± 0.11	2.12 ± 0.03
F(Hβ)[b]				14.25 ± 0.29	1.59 ± 0.03	9.45 ± 0.19	0.43 ± 0.09

Notes. [a]Saturated in the long exposure spectrum.
[b]Flux uncorrected for the reddening in units of 10^{-14} erg cm^{-2} s^{-1}.

4 THE ADDITIONAL SAMPLE

In addition to the Galactic H II regions observed in this paper, we have included the deep spectra of other Galactic objects available from the literature. Most of these nebulae are located at $R_G <11.5$ kpc and only NGC 2579 lies beyond that distance. These objects were selected to compare the results of the anti-centre H II regions with those in the inner Galactic disc. Table 5 gives the most common designation of the additional sample of objects, their Galactocentric distances (see Section 5), their O abundances and the references of their emission-line ratios used for analysis in this paper. The data for M20, M16, M17, M8, NGC 3576, M42, NGC 3603, Sh 2-311 and NGC 2579 were observed with the UVES spectrograph at the VLT, the same instrument configuration as used for the observations of Sh 2-298 included in this paper. The observations of NGC 7635 were obtained with the same instrument configuration as our observations obtained with the GTC OSIRIS spectrograph. The observations of IC 5146, Sh 2-132 and Sh 2-156 produced deep optical spectra obtained with the ISIS spectrograph at the 4.2m *WHT*. Sh 2-132 and Sh 2-156 have been selected from the sample of Galactic anti-centre H II regions observed by Fernández-Martín et al. (2017). We have not considered the rest of the objects observed by those authors because observations of three of them (Sh 2-83, Sh 2-212 and NGC 7635) were also reported by us in this or previous papers, and the rest do not show auroral lines for the determination of T_e in their spectra. The emission line ratios of

IC 5146 were retrieved from García-Rojas, Simón-Díaz & Esteban (2014).

5 DISTANCES

In the studies of Galactic abundance gradients, the distances to H II regions are highly uncertain. However, these uncertainties are usually not taken into account when calculating the radial gradients. The adopted galactocentric distances, R_G, of the objects are presented in Tables 1 and 5. These distances are estimated as the mean values of kinematic and stellar distances given in different published references. Their associated uncertainties correspond to the standard deviation of the values considered for the average. In our distance calculations, we assumed that the Sun is located at $R_G = 8.0$ kpc (Reid 1993). To derive the mean value and standard deviation of R_G for each object, we used the kinematic distances determined by Quireza et al. (2006) and Balser et al. (2011), the stellar ones calculated by Foster & Brunt (2015) and the kinematic and stellar distances calculated or compiled by Russeil (2003) and Caplan et al. (2000). In addition, we have also considered other calculations of the average distance values of NGC 2579, M20, NGC 3576, NGC 3603 and IC 5146. In the case of NGC 2579, we have included the consistent stellar and kinematic distances obtained by Copetti et al. (2007). For M20, we adopted the distance derived from a detailed 3D extinction map by Cambrésy et al. (2011). For IC 5146,

Table 3. Derredened line intensity ratios with respect to $I(\text{H}\,\beta) = 100$ for Sh 2-212, Sh 2-83 and Sh 2-209.

λ_0 (Å)	Ion	ID	$f(\lambda)$	Sh 2-212	$I(\lambda)/I(\text{H}\,\beta)$ Sh 2-83	Sh 2-209
3726	[O II]	1F	0.257	170.9 ± 5.9	76.1 ± 5.7	–
3729	[O II]	1F				
3750	H I	H12	0.253	6.5 ± 1.4	–	–
3771	H I	H11	0.249	9.7 ± 2.2	–	–
3835	H I	H9	0.237	6.1 ± 1.9	–	97 ± 22
3867	He I	20	0.231	9.1 ± 2.7	44.2 ± 4.3	–
3869	[Ne III]	1F				
3889	He I	5	0.227	18.4 ± 2.1	14.2 ± 3.0	–
3889	H I	H8				
3967	[Ne III]	1F	0.211	16.7 ± 2.4	17.8 ± 2.4	–
3970	H I	H7				
4102	H I	H6	0.182	25.0 ± 2.1	23.8 ± 1.7	–
4340	H I	Hγ	0.127	33.9 ± 1.2	45.3 ± 1.3	39.5 ± 2.8
4363	[O III]	2F	0.121	2.48 ± 0.61	4.16 ± 0.50	17.7 ± 3.0
4471	He I	14	0.096	4.61 ± 0.25	4.00 ± 0.36	–
4607	[Fe III]	3F	0.062	0.221 ± 0.052	–	–
4658	[Fe III]	3F	0.050	0.243 ± 0.069	–	–
4711	[Ar IV]	1F	0.037	0.46 ± 0.12	–	–
4713	He I	12	0.036			
4861	H I	Hβ	0.000	100.0 ± 2.1	100.0 ± 2.1	100.0 ± 2.3
4922	He I	48	-0.015	1.433 ± 0.064	1.052 ± 0.088	–
4959	[O III]	1F	-0.024	88.8 ± 1.8	189.0 ± 3.8	92.4 ± 2.0
5007	[O III]	1F	-0.036	265.4 ± 5.3	565 ± 12	276.5 ± 6.1
5016	He I	4	-0.038	2.68 ± 0.24	2.23 ± 0.25	1.50 ± 0.27
5048	He I	47	-0.046		0.206 ± 0.037	–
5518	[Cl III]	1F	-0.154	0.334 ± 0.065	0.610 ± 0.044	0.65 ± 0.15
5538	[Cl III]	1F	-0.158	0.337 ± 0.058	0.420 ± 0.031	0.353 ± 0.085
5755	[N II]	3F	-0.194	0.103 ± 0.026	0.353 ± 0.034	0.530 ± 0.091
5876	He I	11	-0.215	14.04 ± 0.38	12.93 ± 0.40	11.55 ± 0.70
6300	[O I]	1F	-0.282	–	0.791 ± 0.098	–
6312	[S III]	3F	-0.283	0.605 ± 0.063	1.566 ± 0.085	1.11 ± 0.15
6364	O I	1F	-0.291	–	0.144 ± 0.037	–
6548	[N II]	1F	-0.318	2.424 ± 0.062	4.76 ± 0.19	10.30 ± 0.87
6563	H I	Hα	-0.320	280.0 ± 7.2	274 ± 11	259 ± 22
6583	[N II]	1F	-0.323	11.64 ± 0.30	16.08 ± 0.63	31.0 ± 2.7
6678	He I	46	-0.336	2.22 ± 0.25	3.12 ± 0.15	2.98 ± 0.29
6716	[S II]	2F	-0.342	2.08 ± 0.20	4.85 ± 0.20	7.34 ± 0.67
6731	[S II]	2F	-0.344	1.38 ± 0.20	4.26 ± 0.18	6.55 ± 0.60
7065	He I	10	-0.387	1.82 ± 0.17	2.55 ± 0.12	2.18 ± 0.23
7136	[Ar III]	1F	-0.396	11.01 ± 0.33	9.37 ± 0.44	7.67 ± 0.81
7281	He I	45	-0.414	–	0.460 ± 0.048	0.469 ± 0.075
7318	[O II]	2F	-0.418	–	1.276 ± 0.070	1.81 ± 0.30
7320	[O II]	2F				
7330	[O II]	2F	-0.420	–	1.284 ± 0.071	1.74 ± 0.29
7331	[O II]	2F				
7751	[Ar III]	2F	-0.467	–	1.132 ± 0.070	0.84 ± 0.11
$c(\text{H}\,\beta)$				0.93 ± 0.02	2.65 ± 0.05	3.32 ± 0.11
$F(\text{H}\,\beta)^a$				4.98 ± 0.11	11.8 ± 0.2	2.93 ± 0.07

Note. ^{a}Flux uncorrected for reddening in units of 10^{-15} erg cm^{-2} s^{-1}.

García-Rojas et al. (2014) obtained an accurate stellar distance based on their spectroscopic analysis of the ionizing star of the nebula. For NGC 3576 and NGC 3603, we have included the kinematic distances determined by de Pree, Nysewander & Goss (1999). In general, these additional distance determinations are fairly consistent with the stellar and kinematic distances given by Russeil (2003) for each object. Finally, for M42, we adopted the distance obtained from trigonometric parallax (Menten et al. 2007). We have not considered other sources of distances for this last object. From Tables 1 and 5, we can see that the whole sample includes 21 H II regions with direct determinations of T_e that covers a range of Galactocen-

tric distances from 5.1 to 17 kpc, 8 objects with $R_G > R_{25}$ and 13 with $R_G < R_{25}$.

6 RESULTS

For the eight objects in the observed sample, we carried out plasma diagnostics to determine the physical conditions (T_e, N_e) and the ionic abundances based on the line-intensity ratios given in Tables 2–4, using the program PYNEB v1.0.26 (Luridiana, Morisset & Shaw 2015). The atomic data listed in Table 6 are adopted in our spectral analysis. The physical conditions and the ionic and

Table 4. Derredened line intensity ratios with respect to $I(H\beta) = 100$ for Sh 2-298.

λ_0 (Å)	Ion	ID	f(λ)	λ)/I(Hβ)
3721.83	[S III]	2F	0.257	3.63 ± 0.95
3721.94	H I	H14		
3726.03	[O II]	1F	0.257	298.3 ± 9.1
3728.82	[O II]	1F	0.256	417 ± 12
3770.63	H I	H11	0.249	4.35 ± 0.68
3797.90	H I	H10	0.244	4.22 ± 0.34
3819.61	He I	22	0.240	1.51 ± 0.18
3835.39	H I	H9	0.237	5.72 ± 0.42
3868.75	[Ne III]	1F	0.230	96.6 ± 2.7
3889.05	H I	H8	0.226	20.18 ± 0.72
3964.73	He I	5	0.211	0.77 ± 0.18
3967.46	[Ne III]	1F	0.211	29.52 ± 0.90
3970.07	H I	H7	0.210	15.22 ± 0.80
4026.21	He I	18	0.198	1.94 ± 0.21
4068.60	[S II]	1F	0.189	8.80 ± 0.31
4076.35	[S II]	1F	0.187	2.82 ± 0.18
4101.74	H I	H6	0.182	24.77 ± 0.75
4340.47	H I	Hγ	0.127	47.5 ± 1.1
4363.21	[O III]	2F	0.121	6.36 ± 0.28
4387.93	He I	51	0.115	0.72 ± 0.15
4471.48	He I	14	0.096	4.59 ± 0.17
4562.60	[Mg I] ?		0.073	0.96 ± 0.08
4571.09	Mg I] ?		0.071	0.68 ± 0.11
4711.37	[Ar IV]	1F	0.037	0.143 ± 0.024
4713.14	He I	12	0.036	0.501 ± 0.091
4861.33	H I	Hβ	0.000	100.0 ± 2.0
4921.93	He I	48	−0.015	1.27 ± 0.10
4924.5	[Fe III]	2F	−0.016	0.249 ± 0.038
4958.91	[O III]	1F	−0.024	199.5 ± 4.0
5006.84	[O III]	1F	−0.036	598 ± 12
5015.68	He I	4	−0.038	1.61 ± 0.27
5197.90	[N I]	1F	−0.082	1.71 ± 0.29
5200.26	[N I]	1F	−0.083	2.28 ± 0.34
5517.71	[Cl III]	1F	−0.154	0.92 ± 0.19
5537.88	[Cl III]	1F	−0.158	0.80 ± 0.22
5754.64	[N II]	3F	−0.194	3.16 ± 0.26
5875.64	He I	11	−0.215	12.36 ± 0.45
6300.30	[O I]	1F	−0.282	27.32 ± 0.83
6312.10	[S III]	3F	−0.283	3.61 ± 0.21
6347.11	Si II	4	−0.289	0.796 ± 0.085
6363.78	[O I]	1F	−0.291	9.11 ± 0.46
6548.03	[N II]	1F	−0.318	48.9 ± 1.6
6562.82	H I	Hα	−0.320	280.0 ± 9.1
6583.41	[N II]	1F	−0.323	150.7 ± 4.9
6678.15	He I	46	−0.336	3.95 ± 0.33
6716.47	[S II]	2F	−0.342	97.6 ± 3.3
6730.85	[S II]	2F	−0.344	72.5 ± 2.5
7065.28	He I	10	−0.387	2.179 ± 0.098
7135.78	[Ar III]	1F	−0.396	14.12 ± 0.53
7281.35	He I	45	−0.414	0.318 ± 0.074
7318.39	[O II]	2F	−0.418	1.62 ± 0.12
7319.99	[O II]	2F	−0.418	5.03 ± 0.28
7329.66	[O II]	2F	−0.420	2.78 ± 0.18
7330.73	[O II]	2F	−0.420	2.57 ± 0.15
7751.10	[Ar III]	2F	−0.467	3.21 ± 0.15
8467.25	H I	P17	−0.536	0.218 ± 0.062
8665.02	H I	P13	−0.553	0.451 ± 0.072
8727.13	[C I] ?		−0.558	0.160 ± 0.021
8750.47	H I	P12	−0.560	0.660 ± 0.051
8862.79	H I	P11	−0.569	0.857 ± 0.081
9014.91	H I	P10	−0.581	1.20 ± 0.11
9068.90	[S III]	1F	−0.585	18.39 ± 0.94

Table 4 – *continued*

λ_0 (Å)	Ion	ID	f(λ)	λ)/I(Hβ)
9229.01	H I	P9	−0.596	1.69 ± 0.11
9530.60	[S III]	1F	−0.618	66.1 ± 3.5
9545.97	H I	P8	−0.619	1.97 ± 0.16
9850.26	[C I] ?		−0.638	1.83 ± 0.15
10049.40	H I	P7	−0.650	4.05 ± 0.41
c(Hβ)				1.12 ± 0.03
F(Hβ)^a				2.47 ± 0.05

Note. ^{a}Flux uncorrected for the reddening in units of 10^{-14} erg cm^{-2} s^{-1}.

elemental abundances of oxygen of M20, M16, M17, M8, NGC 3576, M42, NGC 3603, Sh 2-311 and NGC 2579 were determined by Esteban, García-Rojas & Pérez-Mesa (2015) using the same procedure and atomic data as for our current sample. The same method was applied to the analysis of NGC 7635, which was published in Esteban et al. (2016b). For IC 5146, Sh 2-132 and Sh 2-156, we recalculated the relevant quantities following the same methodology as for the previous objects and using the line-intensity ratios (as well as uncertainties) retrieved from the references given in Table 5.

6.1 Physical conditions

We have adopted the [S II] λ6717/λ6731 and [Cl III] λ5518/λ5538 density-diagnostic line ratios for all the objects and also added the [O II] λ3726/λ3729 ratio for Sh 2-298. The electron density, N_e, derived from the [S II] line ratio, N_e([S II]), was assumed for all the apertures and objects and it is alway below 1000 cm^{-3} (see Tables 7 and 8). For the singly ionized species, we derived T_e using the [N II] (λ6548+λ6584)/λ5755 nebular-to-auroral line ratio for all objects (see Fig. 4) and the [O II] (λ7319+λ7330)/(λ3726+λ3729) and [S II] (λ4068+λ4076)/(λ6717+λ6731) ratios for some of them. Intensities of the [O II] $\lambda\lambda$7319, 7330 and [N II] λ5755 auroral lines have been corrected for the possible contribution due to the recombination process using the formulae derived by Liu et al. (2000). This contribution is between 0.2 and 13 per cent in the case of the [O II] lines and between 0.07 and 5 per cent for [N II] λ5755. For the doubly ionized species, we have derived T_e using the [O III] (λ4959+λ5007)/λ4363 line ratio for all objects except Sh 2-127 and Sh 2-209, where the [O III] λ4363 auroral line was undetected (see Fig. 5). For these two H II regions, we estimated T_e([O III]) using T_e([N II]) and the empirical relation between the two temperatures given in the equation 3 of Esteban et al. (2009). The [S III] (λ9069+λ9532)/λ6312 line ratio was also measured in Sh 2-298 because the spectrum of this object extends to the near-infrared region. The physical conditions of the H II regions in our observed sample are presented in Tables 7 and 8.

The physical conditions of M20, M16, M17, M8, NGC 3576, M42, NGC 3603, Sh 2-311 and NGC 2579 are presented in table 3 of Esteban et al. (2015), and the physical conditions adopted for the rest of the objects in the additional sample (IC 5146, Sh 2-132, NGC 7635 and Sh 2-156) are given in Table 9. For NGC 7635, the mean values obtained for apertures 2, 3, 4, 5 and 6 observed by Esteban et al. (2016b) were adopted. For IC 5146, we present the average value from apertures 2, 3 and 4 observed by García-Rojas et al. (2014) but recalculated it following the above mentioned procedure and using the atomic data set indicated in Table 6. T_e([O III]) is not quoted for IC 5146 because the [O III] lines were not well detected in its spectrum and its O^{2+}/H$^+$ ratio was negligible. In the case of Sh 2-132 and Sh 2-156, we recalculated their N_e([S II]), T_e([N II]) and

Table 5. Additional sample of H II regions.

H II region	R_G^a (kpc)	$12 + \log(O/H)$	Reference
M20	5.1 ± 0.3	8.51 ± 0.04	García-Rojas et al. (2006)
M16	5.9 ± 0.2	8.54 ± 0.04	García-Rojas, Peña & Peimbert (2009)
M17	6.1 ± 0.2	8.54 ± 0.04	García-Rojas et al. (2007)
M8	6.3 ± 0.8	8.45 ± 0.04	García-Rojas et al. (2007)
NGC 3576	7.5 ± 0.3	8.55 ± 0.04	García-Rojas et al. (2004)
IC 5146	8.10 ± 0.02	8.56 ± 0.04	García-Rojas et al. (2014)
M42	8.34 ± 0.02	8.50 ± 0.04	Esteban et al. (2004)
NGC 3603	8.6 ± 0.4	8.44 ± 0.03	García-Rojas et al. (2006)
Sh 2-132	10.0 ± 0.7	8.35 ± 0.14	Fernández-Martín et al. (2017)
NGC 7635	10.2 ± 0.7	8.40 ± 0.08	Esteban et al. (2016b)
Sh 2-156	10.6 ± 0.6	8.32 ± 0.10	Fernández-Martín et al. (2017)
Sh 2-311	11.1 ± 0.4	8.39 ± 0.01	García-Rojas et al. (2005)
NGC 2579	12.4 ± 0.5	8.26 ± 0.03	Esteban et al. (2013)

Note. ^{a}Galactocentric distances assuming the Sun is at 8 kpc.

Table 6. Atomic data set used for collisionally excited lines.

Ion	Transition probabilities and energy levels	Collisional strengths
N^+	Froese Fischer & Tachiev (2004)	Tayal (2011)
O^+	Froese Fischer & Tachiev (2004)	Kisielius et al. (2009)
O^{2+}	Froese Fischer & Tachiev (2004); Storey & Zeippen (2000)	Storey, Sochi & Badnell (2014)
Ne^{2+}	Galavís, Mendoza & Zeippen (1997)	McLaughlin & Bell (2000)
S^+	Podobedova, Kelleher & Wiese (2009)	Tayal & Zatsarinny (2010)
S^{2+}	Podobedova et al. (2009)	Tayal & Gupta (1999)
Cl^{2+}	Mendoza (1983)	Butler & Zeippen (1989)
Ar^{2+}	Mendoza (1983); Kaufman & Sugar (1986)	Galavís, Mendoza & Zeippen (1995)
Ar^{3+}	Mendoza & Zeippen (1982); Kaufman & Sugar (1986)	Zeippen, Butler & Le Bourlot (1987)
Fe^{2+}	Quinet (1996); Johansson et al. (2000)	Zhang (1996)

T_e([O III]) using the aforementioned procedure and atomic data set. The T_e and N_e values derived for the two last nebulae are consistent with those obtained by Fernández-Martín et al. (2017) within the errors.

6.2 Abundances

The use of large-aperture telescopes, such as the GTC and VLT, allowed us to obtain very deep spectra where the temperature-sensitive faint auroral lines have been well detected in all the objects, which is especially important in the case of the relatively faint H II regions in the Galactic anti-centre. With these data, we have determined ionic abundances from the collisionally excited lines (hereafter CELs). In particular, we derived abundances of N^+, O^+, O^{2+}, S^+, S^{2+}, Cl^{2+} and Ar^{2+} for all the objects in our observed sample; the Ne^{2+}/H^+ ratio was derived for all nebulae except Sh 2-288, Sh 2-127 and Sh 2-209; the Ar^{3+} abundance was derived only in Sh 2-100 and Sh 2-298, and the Fe^{2+} abundance in Sh 2-100, Sh 2-128, Sh 2-288, Sh 2-127 and Sh 2-212. We have also determined the He^+/H^+ ratio for all the observed objects using the relative intensities of recombination lines (herafter RLs). We assumed a two-zone scheme for the calculations of ionic abundances. We adopted T_e([N II]) for the ions with low-ionization potentials (N^+, O^+, S^+ and Fe^{2+}) and T_e([O III]) for the high-ionization species (He^+, O^{2+}, Ne^{2+}, S^{2+}, Cl^{2+}, Ar^{2+} and Ar^{3+}). N_e([S II]) was assumed for all ions. All the computations were made with PYNEB, using the atomic data listed in Table 6.

The He^+/H^+ abundance ratio was determined using PYNEB. Here, the effective recombination coefficients for the He I recombination lines calculated by Porter et al. (2012, 2013), who considered the effects of collisional contribution and the optical depth in the triplet transitions, were adopted. The final adopted He^+/H^+ ratio is a weighted average of the ratios derived from several bright He I lines.

We have detected in the spectrum of Sh 2-100 several RLs of heavy-element ions excited by the pure recombination (see Fig. 6). We derived the C^{2+}/H^+ abundance ratio using the measured flux of the C II λ4267 line, T_e([O III]) and the Case B C II effective recombination coefficients calculated by Davey, Storey & Kisielius (2000). We have determined the O^{+2}/H^+ ratio from the intensity of the O II Multiplet 1 pure RLs. Here, the O II effective recombination coefficients were adopted from the Case B, LS-coupling calculations of Storey (1994) and the T_e([O III]) was assumed. Under typical physical conditions of photoionized nebulae ($N_e \sim 10^2$–10^4), the relative intensities of individual fine-structure lines within the O II M1 multiplet are not constant but varies as a function of the electron density (e.g. Fang & Liu 2013). This is due to the fact that the relative populations of the ground fine-structure levels of the recombining ion (e.g. O^{2+} in the case of O II) deviate from the local thermodynamical equilibrium (LTE), which was seldom considered in previous atomic calculations. We considered this deviation from the LTE by adopting the prescriptions of Peimbert & Peimbert (2005) to apply appropriate correction of the relative strengths of the O II Multiplet 1 lines at densities $N_e < 10^4$ cm^{-3}. The derived ionic abundances

Table 7. Physical conditions and abundances for Sh 2-100, Sh 2-128, Sh 2-288, Sh 2-127 and Sh 2-212.

	Sh 2-100		Sh 2-128	Sh 2-288	Sh 2-127	Sh 2-212
	$t^2 = 0.0$	$t^2 = 0.010$ $\pm\,0.010$	$t^2 = 0.0$	$t^2 = 0.0$	$t^2 = 0.0$	$t^2 = 0.0$
			Physical conditions[a]			
N_e([S II])	430 ± 210		480 ± 90	450 ± 230	600 ± 100	<100
N_e([Cl III])	660 ± 350		700 ± 460	480 ± 380	1430 ± 1070	4200 ± 1900
T_e([N II])	8950 ± 320		$10\,970 \pm 260$	9640 ± 370	9870 ± 170	9760 ± 960
T_e([O II])	$10\,010 \pm 560$		$10\,040 \pm 220$	9990 ± 580	9950 ± 320	...
T_e([S II])	$19\,780 \pm 2450$		...	9700 ± 1040	...	...
T_e([O III])	8140 ± 120		9960 ± 320	9210 ± 490	9610 ± 170^b	$10\,890 \pm 890$
			Ionic abundances[c] and O/H[c] ratio			
He+	11.01 ± 0.01		11.00 ± 0.01	10.82 ± 0.01	10.88 ± 0.01	10.98 ± 0.01
C2+	8.36 ± 0.09		...	...	...	...
N+	6.71 ± 0.05	6.74 ± 0.06	6.76 ± 0.02	7.17 ± 0.05	7.28 ± 0.02	6.31 ± 0.09
O+	7.64 ± 0.11	7.68 ± 0.11	7.77 ± 0.05	8.16 ± 0.11	8.19 ± 0.05	7.84 ± 0.25
O2+(CELs)	8.45 ± 0.02	8.52 ± 0.06	7.98 ± 0.04	7.75 ± 0.07	7.38 ± 0.03	7.85 ± 0.09
O2+(RLs)	8.52 ± 0.06		...	...	...	...
Ne2+	7.76 ± 0.06	7.84 ± 0.10	7.04 ± 0.14	...	...	6.85 ± 0.32
S+	5.87 ± 0.07	5.90 ± 0.07	5.58 ± 0.03	5.91 ± 0.11	5.91 ± 0.02	4.97 ± 0.12
S2+	6.94 ± 0.07	7.02 ± 0.10	6.52 ± 0.08	6.63 ± 0.16	6.69 ± 0.07	5.99 ± 0.21
Cl2+	5.07 ± 0.03	5.14 ± 0.08	4.78 ± 0.05	4.76 ± 0.08	4.76 ± 0.06	4.53 ± 0.13
Ar2+	6.30 ± 0.07	6.36 ± 0.09	5.88 ± 0.04	5.81 ± 0.11	5.76 ± 0.03	5.92 ± 0.09
Ar3+	4.83 ± 0.12	4.90 ± 0.13	...	...	...	...
Fe2+	5.30 ± 0.04	5.37 ± 0.09	5.71 ± 0.06	5.78 ± 0.05	5.56 ± 0.04	4.95 ± 0.28
O	8.52 ± 0.03	8.58 ± 0.05	8.19 ± 0.03	8.31 ± 0.08	8.25 ± 0.04	8.15 ± 0.12

Notes. [a]N_e in cm^{-3}; T_e in K.
[b]Estimated from T_e([N II]) and equation 3 in Esteban et al. (2009).
[c]In the logarithmic scale $12 + \log(X^{n+}/H^+)$.

Table 8. Physical conditions and abundances for Sh 2-83, Sh 2-209 and Sh 2-298.

	Sh 2-83	Sh 2-209	Sh 2-298
		Physical conditions[a]	
N_e([S II])	300 ± 100	310 ± 200	<100
N_e([O II])	...	...	<100
N_e([Cl III])	<100	<100	1100^{+2100}_{-1100}
T_e([N II])	$12\,840 \pm 660$	$10\,650 \pm 870$	$11\,850 \pm 490$
T_e([O II])	$13\,670 \pm 890$	...	$10\,060 \pm 200$
T_e([S II])	...	...	$12\,580 \pm 450$
T_e([O III])	$11\,490 \pm 490$	$10\,710^b \pm 870$	$11\,720 \pm 200$
T_e([S III])	...	...	$15\,340 \pm 700$
		Ionic abundances[c] and O/H[c] ratio	
He+	10.94 ± 0.01	10.89 ± 0.02	10.96 ± 0.01
N+	6.24 ± 0.04	6.73 ± 0.09	7.31 ± 0.04
O+	7.05 ± 0.12	7.66 ± 0.23	8.12 ± 0.02
O2+	8.10 ± 0.05	7.89 ± 0.09	8.10 ± 0.02
Ne2+	7.45 ± 0.12	...	7.76 ± 0.03
S+	5.14 ± 0.05	5.50 ± 0.09	6.49 ± 0.06
S2+	6.31 ± 0.10	6.28 ± 0.23	6.46 ± 0.02
Cl2+	4.63 ± 0.06	4.70 ± 0.16	4.83 ± 0.09
Ar2+	5.69 ± 0.05	5.65 ± 0.09	5.95 ± 0.02
Ar3+	...	...	4.32 ± 0.02
O	8.14 ± 0.05	8.09 ± 0.10	8.41 ± 0.02

Notes. [a]N_e in cm^{-3}; T_e in K.
[b]Estimated from T_e([N II]) and equation 3 in Esteban et al. (2009).
[c]Assuming $t^2 = 0.0$. In the logarithmic scale $12 + \log(X^{n+}/H^+)$.

for our targets, as well the uncertainties, are presented in Tables 7 and 8.

As we can see in Table 7, the O^{2+}/H^+ abundance ratio derived from the RLs for Sh 2-100 is higher than the abundances determined from the CELs. This is a common observational fact in all H II regions where the O^{2+}/H^+ and C^{2+}/H^+ ratios can be determined using both CELs and RLs. This is called the abundance discrepancy problem and its origin is still under debate (e.g. García-Rojas &
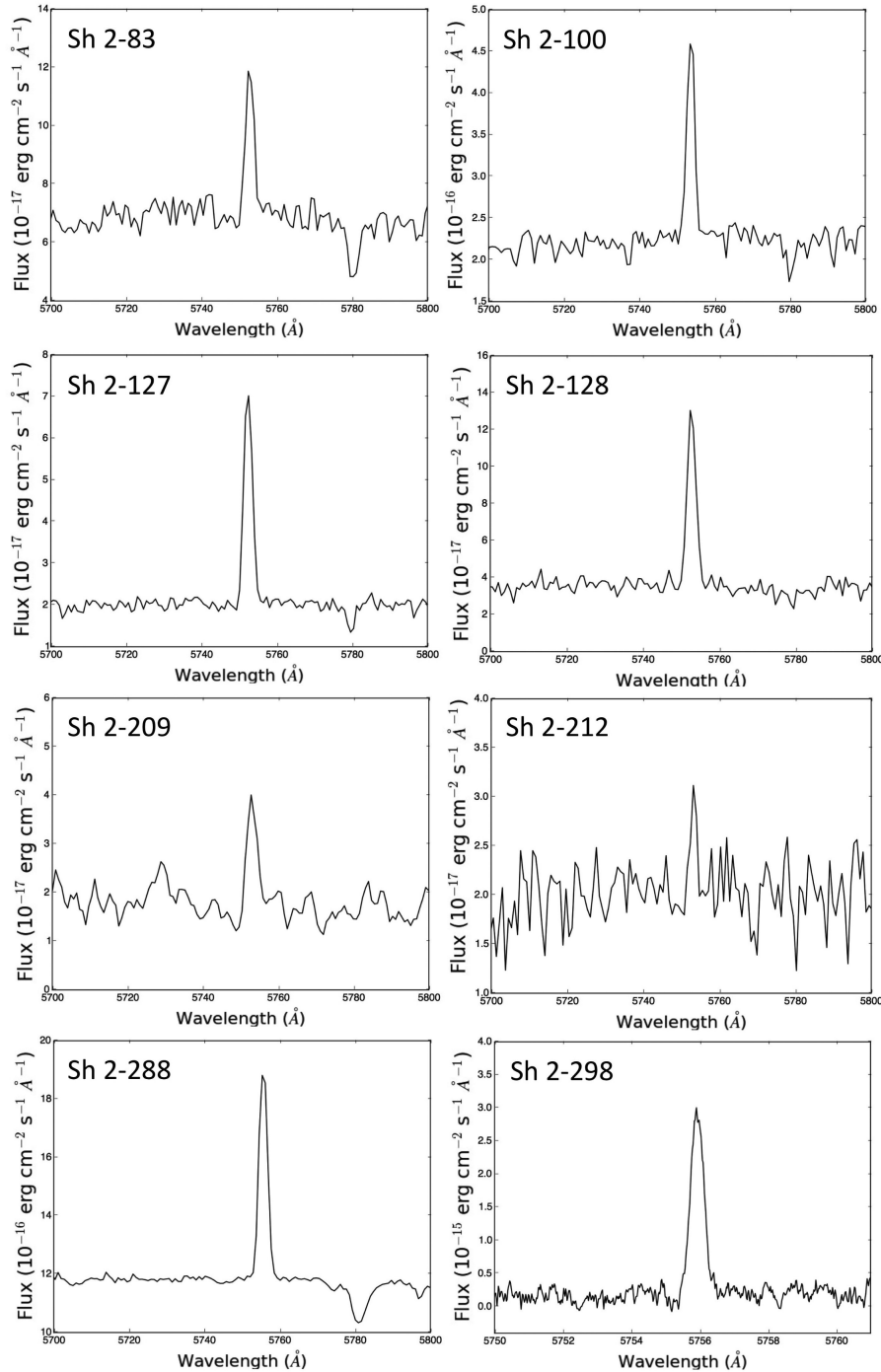
Figure 4. Section of the spectrum of Sh 2-83, Sh 2-100, Sh 2-127, Sh 2-128, Sh 2-209, Sh 2-212, Sh 2-288 and Sh 2-298 showing the [N II] λ5755 auroral line.

Esteban 2007; Esteban, Toribio San Cipriano & García-Rojas 2016a). For Sh 2-100, the ratio of the two O^{2+}/H^+ abundances determined from RLs and CELs, defined as the abundance discrepancy factor (ADF), is 0.07 dex, which is one of the lowest values ever found in H II regions. This is also slightly lower than the ADF found in the Orion nebula (see Esteban et al. 2016a). Assuming that the abundance discrepancy is due to the presence of fluctuations in the spatial distribution of T_e inside the nebula (Torres-Peimbert, Peimbert & Daltabuit 1980), we can estimate the temperature fluctuation parameter t^2, which was first defined by Peimbert (1967) to

reconcile the O^{2+}/H^+ abundance ratios determined from RLs and CELs. The t^2 value we obtained for Sh 2-100 is 0.010 ± 0.010. We considered two sets of abundances for this object, one for the case of $t^2 = 0$ and the other for $t^2 = 0.010 \pm 0.010$. We could not derive t^2 for the other H II regions in our sample. Therefore, their abundances were only calculated for $t^2 = 0$.

Since the aim of this paper is to explore the slope of the Galactic radial gradient of oxygen in the anti-centre direction, we limit our study to determine the total abundances of oxygen. In H II regions, O is the only element for which no ionization correction factor
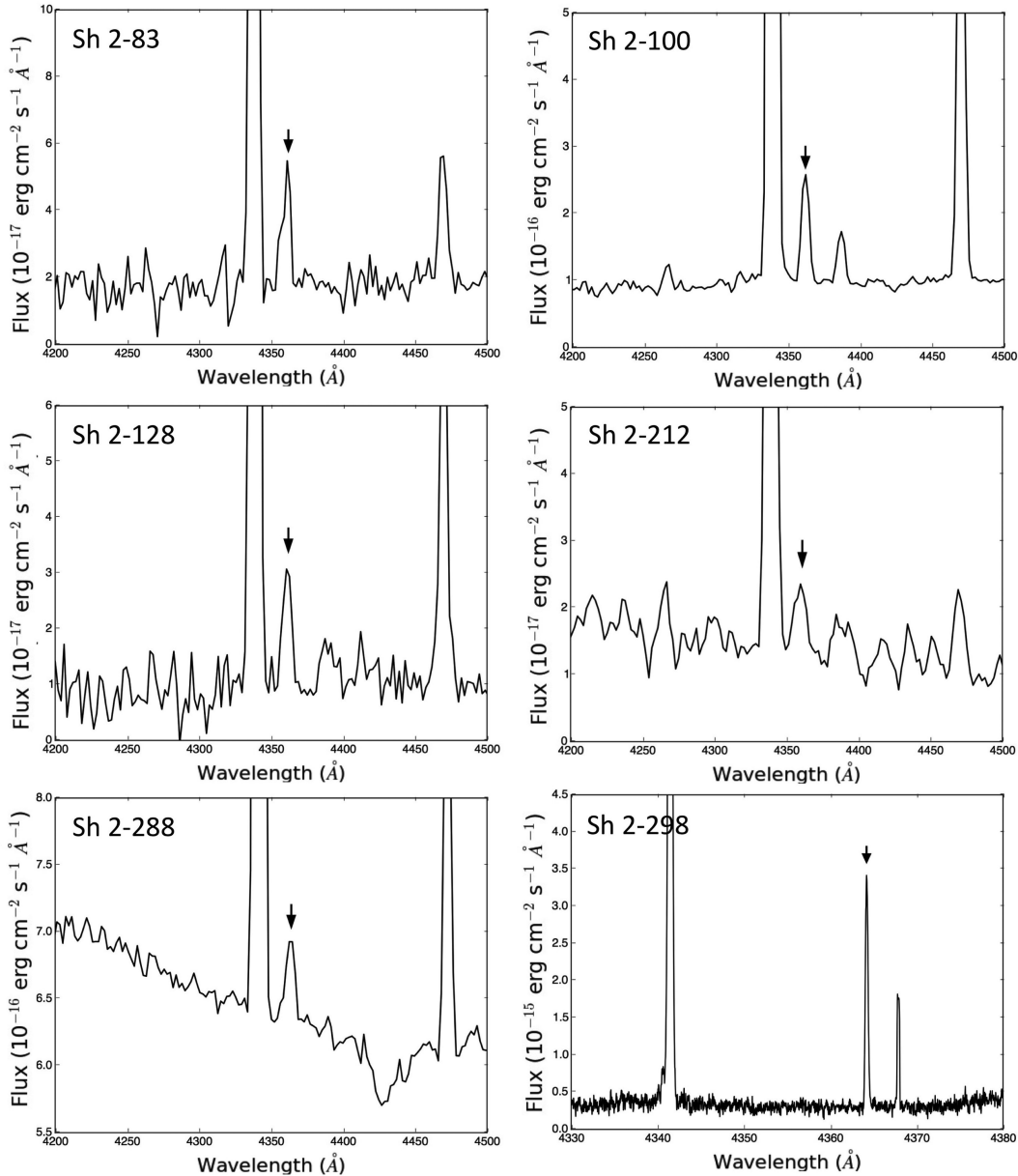
Figure 5. Section of the spectrum of Sh 2-83, Sh 2-100, Sh 2-128, Sh 2-212, Sh 2-288 and Sh 2-298 showing the [O III] λ4363 auroral line (indicated by an arrow).

(hereafter ICF) is needed to derive its total abundance; therefore its calculation is more accurate than for other elements. The total O abundance is simply the sum of the O^+/H^+ and O^{2+}/H^+ ratios. We could also estimate the total abundances of He, N, Ne, S, Cl, Ar and Fe for our objects, but we need ICFs, which are empirically derived based on the similarity of ionization potentials of different ionic species or estimated from photoionization models. We plan to study the gradients of these elements in a future paper where we will carry out a critical analysis of the best ICFs for each element, including additional observations for the nebulae with accurate determinations of the N abundance. As it has been said before, we detect the very faint C II λ4267 RL in the spectrum of Sh 2-100, and this is a remarkable result considering the paucity of determinations of C abundance in Galactic H II regions. As for the rest of the elements – apart from O – we will present the C abundance of this object as well as a reassessment of the Galactic gradient of C/H in a future paper.

In Table 9, we present the recalculated values of the O abundances for IC 5146, Sh 2-132, NGC 7635 and Sh 2-156. The O/H ratios of M20, M16, M17, M8, NGC 3576, M42, NGC 3603, Sh 2-311 and NGC 2579 are presented in table 7 of Esteban et al. (2015).

7 THE O GRADIENT AT THE ANTI-CENTRE

As indicated in Section 1, Fernández-Martín et al. (2017) recently studied the chemical composition of a sample of H II regions in the Galactic anti-centre. We developed the observational program prior to the publication of that paper. Fernández-Martín et al. (2017) detected auroral lines to derive T_e in five objects of their sample. Of those five objects, two are included in our current sample, Sh 2-83 and Sh 2-212, and a third one, Sh 2-162, corresponds to our NGC 7635, for which we recalculated T_e and the O/H ratio from the emission line ratios measured by Esteban et al. (2016b) in their

Table 9. T_e, N_e and abundances recalculated for IC 5146, Sh 2-132, NGC 7635 and Sh 2-156.

	IC 5146[a]	Sh 2-132	NGC 7635[b]	Sh 2-156
N_e([S II]) (cm^{-3})	<100	260 ± 10	160 ± 100	900 ± 25
T_e([N II]) (K)	7140 ± 120	9350 ± 460	8390 ± 390	9460 ± 400
T_e([O III]) (K)	···	8870[c] ± 460	8190 ± 510	9010 ± 350
12+log(O/H)	8.56 ± 0.04	8.35 ± 0.14	8.40 ± 0.08	8.32 ± 0.10

Notes. [a]Mean of the values of apertures 2, 3 and 4 observed by García-Rojas et al. (2014).
[b]Mean of the values of apertures 2, 3, 4, 5 and 6 observed by Esteban et al. (2016b).
[c]Estimated from T_e([N II]) and equation 3 of Esteban et al. (2009).
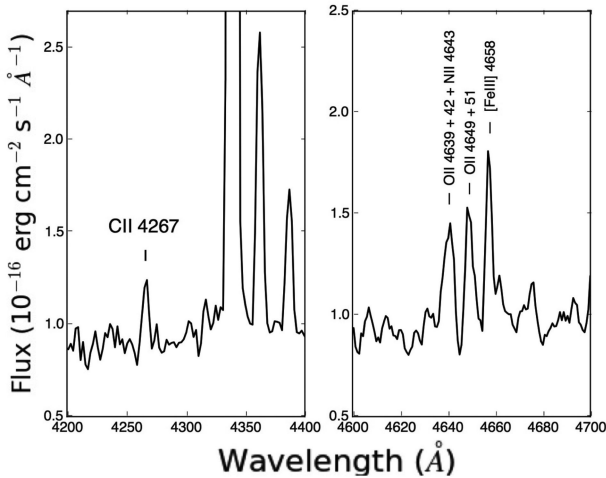
Figure 6. Sections of the spectrum of Sh 2-100 showing the C II λ4267 (left) and O II Multiplet 1 λ4650 (right) optical recombination lines.

deeper spectra taken at the GTC. The other two objects for which Fernández-Martín et al. (2017) determined T_e are Sh 2-132 and Sh 2-156. The authors collected spectra of additional H II regions taken from the literature and all of them correspond to observations obtained at 2–4 m telescopes and published between 1979 and 2000. When describing the procedure of data collection from the literature, Fernández-Martín et al. (2017) stated that they *carried out an exhaustive bibliographical review* of spectroscopical results of H II regions located at R_G >11 kpc. It is surprising that they overlooked the deepest observations of this kind of objects published prior to 2016: the VLT spectroscopy of Sh 2-311 and NGC 2579 published by García-Rojas et al. (2005) and Esteban et al. (2013), respectively. Moreover, for Sh 2-311, Fernández-Martín et al. (2017) instead of using the far much better quality data by García-Rojas et al. (2005) adopted the emission line ratios obtained by Shaver et al. (1983) with the 3.6 m telescope and the 3.9 m AAT at La Silla and Siding Spring, respectively. We consider that the new data presented in this paper in combination with (a) the compilation of deep spectroscopy from the literature (all of them except one obtained from 8-10 m telescopes) and (b) the recalculations of the abundances in a homogeneous way are a substantial improvement in the exploration of the true shape of the O abundance gradient at the Galactic anti-centre.

We performed a least-squares linear fit to the oxygen abundance as a function of R_G for the whole sample, including objects in the Galactic anti-centre and the inner disc, i.e. all the objects included in Tables 7–9 which cover R_G of 5.1–17 kpc. The fits give the

following radial O abundance gradient:

$$12 + \log(O/H) = 8.79(\pm 0.05) - 0.040(\pm 0.005)R_G, \quad (1)$$

where the uncertainties are estimated through Monte Carlo simulations. We generated 10^4 random values of R_G and the O abundance for each observational data point assuming a Gaussian distribution with a sigma equal to the measurement uncertainty of each quantity. We performed a least-squares linear fit to each of these 10^4 random distributions. The uncertainties associated with the slope and intercept correspond to the standard deviation of the values of these two quantities obtained from the fits. The spatial distribution of the O abundances and the gradient are shown in Fig. 7. Using a similar methodology, Esteban et al. (2015) determined a slope of −0.043 dex kpc^{-1} for the O gradient defined by a subset of our sample of H II regions restricted to R_G ≤12.4 kpc. The most recent determinations of the Galactic gradient of oxygen for the whole disc available in the literature show consistent slopes: Deharveng et al. (2000) obtained a slope of −0.040(±0.005) dex kpc^{-1}; Quireza et al. (2006) derived −0.043(±0.007) dex kpc^{-1}; Rudolph et al. (2006) gave −0.060(±0.010) and −0.042(±0.013) dex kpc^{-1}, when they used the optical and far-infrared lines, respectively; Balser et al. (2011) presented a slope of −0.045(±0.005) dex kpc^{-1}. As we can see, these determinations are highly consistent, indicating that the slope of the radial abundance gradient of oxygen has been well established for the Milky Way.

The average difference between the oxygen abundances of the H II regions represented in Fig. 7 and those given by the linear fit at their corresponding galactocentric distances is ±0.05 dex, similar order of the average uncertainty of the abundance determinations. The maximum difference we find is ±0.10 dex. This is an upper limit of any local inhomogeneity of the O abundance that is consistent with our results.

In order to explore whether a change of the slope of the oxygen gradient is present in the outer disc, we carried out additional least-square fits separately to the H II regions within and beyond R_{25} (= 11.5 kpc). The radial O gradient we found for the objects within R_{25} is

$$12 + \log(O/H) = 8.70(\pm 0.07) - 0.029(\pm 0.009)R_G \quad (2)$$

and that for the external H II regions ($R_G > R_{25}$) is

$$12 + \log(O/H) = 8.87(\pm 0.23) - 0.046(\pm 0.017)R_G. \quad (3)$$

All these gradients are presented in Fig. 7. As we can see in the figure and ascertain by comparing the parameters of the gradients, their slopes are consistent within the uncertainties, indicating that the shape of the gradient does not change substantially across the Galactic disc. Therefore, our results confirm the absence of flattening in the radial O abundance gradient beyond R_{25}, at least up to R_G ~17 kpc or ~1.5 × R_{25}. As a conclusion, we can say that inside-out models of galaxy formation are also valid to explain the chemical composition of the outer parts of the Milky Way.

In Fig. 7, we also present the average O abundances of the Large and Small Magellanic Clouds (hereafter LMC and SMC) obtained by Toribio San Cipriano et al. (2017) and Domínguez-Guzmán et al. (2017) from deep echelle spectra of a sample of H II regions obtained with the VLT. We can see that the ionized gas-phase abundances of O in the outer regions (beyond R_{25}) of the Milky Way is between the values measured in the Magellanic Clouds. Abundances of the outermost H II regions are closer to the low value observed in the SMC. The slope of the oxygen gradient obtained by Fernández-Martín et al. (2017) for the R_G from 11 to 18 kpc is between −0.053
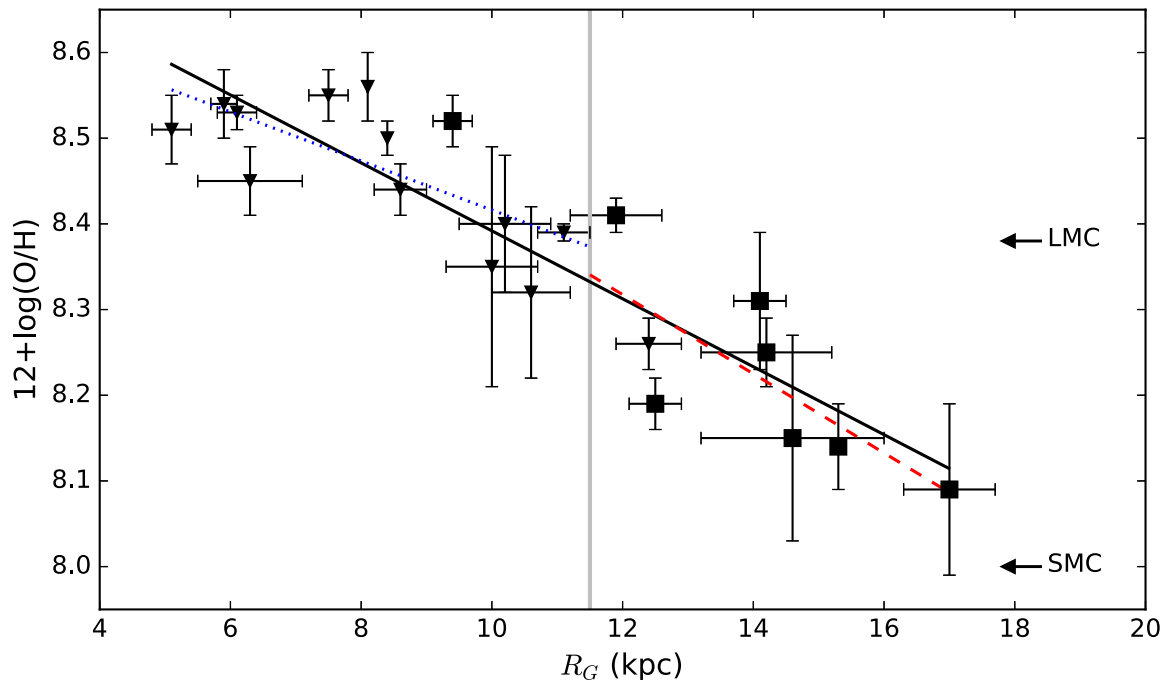
Figure 7. Radial distribution of the oxygen abundance, in logarithm 12+log(O/H), as a function of the Galactocentric distance, R_G, for the whole sample of Galactic H II regions. Large filled squares represent the objects of our current sample and small filled triangles indicate the additional sample. The solid black line is a least-squares linear fit to all objects. The vertical grey line marks the position of the isophotal radius of the Milky Way, $R_{25} = 11.5$ kpc (de Vaucouleurs & Pence 1978). The blue dotted line is a least-squares linear fit to the H II regions located at $R_G < R_{25}$ and the red dashed line is the fit to those at $R_G > R_{25}$. The figure graphically demonstrates that the slope of the gradient does not change significantly across the Galactic disc and the lack of flattening in the outer zone. The arrows indicate the average O abundances of H II regions in the LMC and SMC (Domínguez-Guzmán et al. 2017; Toribio San Cipriano et al. 2017).

and -0.061 dex kpc^{-1}, consistent with our determinations for the outer disc within the uncertainties.

We have investigated O gradients – in the Milky Way and other nearby galaxies – in other papers of our group (Esteban et al. 2005, 2013; Toribio San Cipriano et al. 2016, 2017), always focusing on the gradient derived from O abundances determined from RLs. One question that we want to briefly address is the possible effect of the abundance discrepancy or the presence of temperature fluctuations in the abundance gradient derived in this paper. García-Rojas & Esteban (2007) and Esteban et al. (2016a) found that H II regions in the discs of spiral galaxies where the ADF has been calculated show quite similar values of such quantity. In fact, García-Rojas & Esteban (2007) found that the ADF seemed to be independent of some basic properties of H II regions, i.e. metallicity or T_e. Moreover, the O/H gradients determined from CELs and RLs are almost identical. Some indication of a possible correlation between the ADF and the O/H ratio determined from CELs has appeared with the latest results on low-metallicity objects obtained by Toribio San Cipriano et al. (2017). This correlation indicates that objects with a lower O/H ratio seem to show higher values of the ADF, but this is only apparent for objects with 12+log(O/H) $\leq$ 8.1. Taking into account that our objects show O/H ratios – determined from CELs – larger than that value, we do not consider that this effect may be affecting to the H II regions studied in this paper.

8 CONCLUSIONS

We present very deep optical spectra of eight H II regions located in the anti-centre of the Milky Way, with R_G between 9.4 and 17 kpc. The data were obtained at the 10.4m GTC and the 8.2m VLT. We derived T_e([N II]) for all the objects and T_e([O III]) for six

of them. This permits to use the direct-T_e method based on the measurements of the temperature-sensitive auroral lines to derive chemical abundances. We also included an additional sample of 13 H II regions located in the inner and outer disc of the Milky Way, whose spectra were also obtained with large telescopes. Reliable electron temperatures were also determined for these additional objects. The physical conditions and ionic abundances of all objects were derived using the same methodology and atomic data set. We also detected the C II and O II optical recombination lines in Sh 2-100, for which we calculated the abundance discrepancy factor in O^{2+}. This factor is higher than unity but rather small.

We derived the oxygen abundances for all objects, thus allowing the determination of the radial abundance gradient over a wide range of R_G, from 5.1 to 17 kpc. Eight objects are located outside of R_{25} and 13 inside R_{25}. A least-squares linear fit to the oxygen abundance gradient of the whole sample, including the H II regions in the outer and inner Galactic disc, gives a slope of -0.040 ± 0.005 dex kpc^{-1}. Additional least-squares fits of the inner and outer disc objects, separated by $R_{25} = 11.5$ kpc, give similar slopes. In particular, the slope of the H II regions located beyond R_{25} is -0.046 ± 0.017 dex kpc^{-1}. This result indicates that there is no evidence of flattening in the radial O abundance gradient beyond R_{25}, at least up to 17 kpc ($\sim 1.5 \times R_{25}$). In general, we find that the scatter in the O/H ratios of H II regions across the Galactic disc is not substantially larger than the observational uncertainties, with the largest possible inhomogeneities of the order of 0.1 dex.

In an appendix, we explored the radial distribution of T_e([O III]) and T_e([N II]) across the Galactic disc and found gradients with similar positive slopes for both temperatures, with much larger scatter in T_e([N II]). The shape of the T_e gradients is consistent with

the absence of flattening in the metallicity gradient in the outer Galactic disc.

The results of this work indicate that the inside-out models of galaxy formation are also valid to explain the chemical composition of the outer regions of the Milky Way.

ACKNOWLEDGEMENTS

REFERENCES

Balser D. S., Rood R. T., Bania T. M., Anderson L. D., 2011, ApJ, 738, 27

Bohlin R. C., Lindler D., 1992, STScI Newsl., 9, 19

Bresolin F., 2016, in Knapen J. H., Lee J. C., Gil de Paz A., eds, Outskirts of Galaxies. Springer, Berlin

Bresolin F., Ryan-Weber E., Kennicutt R. C., Goddard Q., 2009, ApJ, 695, 580

Bresolin F., Kennicutt R. C., Ryan-Weber E., 2012, ApJ, 750, 122

Butler K., Zeippen C. J., 1989, A&A, 208, 337

Cambrésy L., Rho J., Marshall D. J., Reach W. T., 2011, A&A, 527, A141

Caplan J., Deharveng L., Peña M., Costero R., Blondel C., 2000, MNRAS, 311, 317

Cardelli J. A., Clayton G. C., Mathis J. S., 1989, ApJ, 345, 245

Cepa J. et al., 2000, in Iye M., Moorwood A. F., eds, Proc. SPIE Conf. Ser. Vol. 4008, Optical and IR Telescope Instrumentation and Detectors. SPIE, Bellingham, p. 623

Cepa J. et al., 2003, in Iye M., Moorwood A. F. M., eds, Proc. SPIE Conf. Ser. Vol. 4841, Instrument Design and Performance for Optical/Infrared Ground-based Telescopes. SPIE, Bellingham, p. 1739

Churchwell E., Walmsley C. M., 1975, A&A, 38, 451

Copetti M. V. F., Oliveira V. A., Riffel R., Castañeda H. O., Sanmartim D., 2007, A&A, 472, 847

Davey A. R., Storey P. J., Kisielius R., 2000, A&AS, 142, 85

de Pree C. G., Nysewander M. C., Goss W. M., 1999, AJ, 117, 2902

de Vaucouleurs G., Pence W. D., 1978, AJ, 83, 1163

Deharveng L., Peña M., Caplan J., Costero R., 2000, MNRAS, 311, 329

D'Odorico S., Cristiani S., Dekker H., Hill V., Kaufer A., Kim T., Primas F., 2000, Proc. SPIE, 4005, 121

Domínguez-Guzmán G., Rodríguez M., Esteban C., García-Rojas J., 2017, in Hägele G., Cardaci M., Pérez-Montero E., eds, Chemical Abundances in Ionized Nebulae. Vol. 12, Asociación Argentina de Astronomía, Buenos Aires

Drissen L., 1999, in van der Hucht K. A., Koenigsberger G., Eenens P. R. J., eds, Proc. IAU Symp. Vol. 193, Wolf-Rayet Phenomena in Massive Stars and Starburst Galaxies. Astronomical Society of the Pacific, San Francisco, p. 403

Esteban C., Peimbert M., García-Rojas J., Ruiz M. T., Peimbert A., Rodríguez M., 2004, MNRAS, 355, 229

Esteban C., García-Rojas J., Peimbert M., Peimbert A., Ruiz M. T., Rodríguez M., Carigi L., 2005, ApJ, 618, L95

Esteban C., Bresolin F., Peimbert M., García-Rojas J., Peimbert A., Mesa-Delgado A., 2009, ApJ, 700, 654

Esteban C., Carigi L., Copetti M. V. F., García-Rojas J., Mesa-Delgado A., Castañeda H. O., Péquignot D., 2013, MNRAS, 433, 382

Esteban C., García-Rojas J., Pérez-Mesa V., 2015, MNRAS, 452, 1553

Esteban C., Toribio San Cipriano L., García-Rojas J., 2016a, in Hägele G., Cardaci M., Pérez-Montero E., eds, Chemical Abundances in Ionized Nebulae. Vol. 12, Asociación Argentina de Astronomía, Buenos Aires.

Esteban C., Mesa-Delgado A., Morisset C., García-Rojas J., 2016b, MNRAS, 460, 4038

Fang X., Liu X.-W., 2013, MNRAS, 429, 2791

Fang X., García-Benito R., Guerrero M. A., Liu X., Yuan H., Zhang Y., Zhang B., 2015, ApJ, 815, 69

Fernández-Martín A., Pérez-Montero E., Vílchez J. M., Mampaso A., 2017, A&A, 597, A84

Fich M., Silkey M., 1991, ApJ, 366, 107

Foster T., Brunt C. M., 2015, AJ, 150, 147

Froese Fischer C., Tachiev G., 2004, At. Data Nucl. Data Tables, 87, 1

Galavís M. E., Mendoza C., Zeippen C. J., 1995, A&AS, 111, 347

Galavís M. E., Mendoza C., Zeippen C. J., 1997, A&AS, 123, 159

García-Rojas J., Esteban C., 2007, ApJ, 670, 457

García-Rojas J., Esteban C., Peimbert M., Rodríguez M., Ruiz M. T., Peimbert A., 2004, ApJS, 153, 501

García-Rojas J., Esteban C., Peimbert A., Peimbert M., Rodríguez M., Ruiz M. T., 2005, MNRAS, 362, 301

García-Rojas J., Esteban C., Peimbert M., Costado M. T., Rodríguez M., Peimbert A., Ruiz M. T., 2006, MNRAS, 368, 253

García-Rojas J., Esteban C., Peimbert A., Rodríguez M., Peimbert M., Ruiz M. T., 2007, Rev. Mex. Astron. Astrofis., 43, 3

García-Rojas J., Peña M., Peimbert A., 2009, A&A, 496, 139

García-Rojas J., Simón-Díaz S., Esteban C., 2014, A&A, 571, A93

Garnett D. R., 1992, AJ, 103, 1330

Hamann W.-R., Gräfener G., Liermann A., 2006, A&A, 457, 1015

Henry R. B. C., Kwitter K. B., Jaskot A. E., Balick B., Morrison M. A., Milingo J. B., 2010, ApJ, 724, 748

Johansson S., Zethson T., Hartman H., Ekberg J. O., Ishibashi K., Davidson K., Gull T., 2000, A&A, 361, 977

Kaufman V., Sugar J., 1986, J. Phys. Chem. Ref. Data, 15, 321

Kisielius R., Storey P. J., Ferland G. J., Keenan F. P., 2009, MNRAS, 397, 903

Lemasle B. et al., 2013, A&A, 558, A31

Lépine J. R. D. et al., 2011, MNRAS, 417, 698

Liu X.-W., Storey P. J., Barlow M. J., Danziger I. J., Cohen M., Bryce M., 2000, MNRAS, 312, 585

Luck R. E., Gieren W. P., Andrievsky S. M., Kovtyukh V. V., Fouqué P., Pont F., Kienzle F., 2003, A&A, 401, 939

Luridiana V., Morisset C., Shaw R. A., 2015, A&A, 573, A42

Maciel W. J., Lago L. G., Costa R. D. D., 2006, A&A, 453, 587

McLaughlin B. M., Bell K. L., 2000, J. Phys. B: At. Mol. Opt. Phys., 33, 597

Mendoza C., 1983, in Flower D. R., ed., Proc. IAU Symp. Vol. 103, Planetary Nebulae. D. Reidel Publishing Co., Dordrecht, p. 143

Mendoza C., Zeippen C. J., 1982, MNRAS, 198, 127

Menten K. M., Reid M. J., Forbrich J., Brunthaler A., 2007, A&A, 474, 515

Pedicelli S. et el., 2009, A&A, 504, 81

Peimbert M., 1967, ApJ, 150, 825

Peimbert A., Peimbert M., 2005, Rev. Mex. Astron. Astrofis., 23, 9

Peimbert M., Torres-Peimbert S., Rayo J. F., 1978, ApJ, 220, 516

Podobedova L. I., Kelleher D. E., Wiese W. L., 2009, J. Phys. Chem. Ref. Data, 38, 171

Porter R. L., Ferland G. J., Storey P. J., Detisch M. J., 2012, MNRAS, 425, L28

Porter R. L., Ferland G. J., Storey P. J., Detisch M. J., 2013, MNRAS, 433, L89

Quinet P., 1996, A&AS, 116, 573

Quireza C., Rood R. T., Bania T. M., Balser D. S., Maciel W. J., 2006, ApJ, 653, 1226

Reid M. J., 1993, ARA&A, 31, 345

Rudolph A. L., Fich M., Bell G. R., Norsen T., Simpson J. P., Haas M. R., Erickson E. F., 2006, ApJS, 162, 346

Russeil D., 2003, A&A, 397, 133

Sánchez S. F. et al., 2014, A&A, 563, A49

Shaver P. A., McGee R. X., Newton L. M., Danks A. C., Pottasch S. R., 1983, MNRAS, 204, 53

Storey P. J., 1994, A&A, 282, 999

Storey P. J., Hummer D. G., 1995, MNRAS, 272, 41

Storey P. J., Zeippen C. J., 2000, MNRAS, 312, 813

Storey P. J., Sochi T., Badnell N. R., 2014, MNRAS, 441, 3028

Tayal S. S., 2011, ApJS, 195, 12

Tayal S. S., Gupta G. P., 1999, ApJ, 526, 544

Tayal S. S., Zatsarinny O., 2010, ApJS, 188, 32

Toribio San Cipriano L., García-Rojas J., Esteban C., Bresolin F., Peimbert M., 2016, MNRAS, 458, 1866

Toribio San Cipriano L., Domínguez-Guzmán G., Esteban C., García-Rojas J., Mesa-Delgado A., Bresolin F., Rodríguez M., Simón-Díaz S., 2017, MNRAS, 467, 3759

Torres-Peimbert S., Peimbert M., Daltabuit E., 1980, ApJ, 238, 133

Turnshek D. A., Bohlin R. C., Williamson R. L., Lupie O. L., Koornneef J., Morgan D. H., 1990, AJ, 99, 1243

Vale Asari N., Stasińska G., Morisset C., Cid Fernandes R., 2016, MNRAS, 460, 1739

Vílchez J. M., Esteban C., 1996, MNRAS, 280, 720

Vlajić M., Bland-Hawthorn J., Freeman K. C., 2011, ApJ, 732, 7

Yong D., Carney B. W., Friel E. D., 2012, AJ, 144, 95

Zeippen C. J., Butler K., Le Bourlot J., 1987, A&A, 188, 251

Zhang H., 1996, A&AS, 119, 523

APPENDIX A: THE T_e GRADIENT

The presence of a radial gradient of T_e in the Milky Way is well established from the radio continuum emission observations (e.g. Churchwell & Walmsley 1975; Shaver et al. 1983; Quireza et al. 2006) and the optical [O III] emission line ratios (e.g. Peimbert, Torres-Peimbert & Rayo 1978; Deharveng et al. 2000). Heavy elements such as O or N are the main coolants of photoionized gas and therefore the T_e of H II regions is related to its metallicity. Consequently, we expect to find T_e gradients in the Milky Way and in other galaxies. In this paper, we have derived the T_e([O III]) and T_e([N II]) for a number of H II regions in the outer disc of the Galaxy and compiled/recalculated these temperatures for additional objects in the inner Galactic disc. In total, we obtained 17 determinations of the T_e([O III]) and 20 T_e([N II]), which are presented in Tables 7–9 in this paper and table 3 in Esteban et al. (2015).

In Fig. A1, we show the radial distribution of T_e([O III]) and T_e([N II]) of the H II regions of our complete sample. Our least-squares linear fit to the T_e([O III]) of the whole sample gives

$$T_e([\text{O III}]) = 5900(\pm 320)\text{K} + 320(\pm 40) \times R_G; \qquad (A1)$$

and our fit to the T_e([N II]) gives

$$T_e([\text{N II}]) = 7110(\pm 360)\text{K} + 240(\pm 40) \times R_G. \qquad (A2)$$

The derived slope of the T_e([O III]) radial gradient, 320 ± 40 K kpc^{-1}, is fairly close to the values of 372 ± 38 and 287 ± 46 K kpc^{-1} determined by Deharveng et al. (2000) and Quireza et al. (2006), respectively. The average difference between the T_e([O III]) of the H II regions in Fig. A1 and the value derived from the linear fit at their corresponding distances is 530 K, not much larger than the average uncertainty (300 K) of the T_e([O III]) determinations. The maximum difference is 2040 K found in Sh 2-298, an H II region with the hottest ionizing star in our sample. The ionizing source of Sh 2-298 is the Wolf–Rayet (WR) star HD 56925, which has been classified as WN4, with $T_{\text{eff}} \sim 112\,200$ K (Hamann, Gräfener & Liermann 2006). Normal H II regions are usually ionized by OB stars with T_{eff} between 30 000 and 45 000 K. We have recalculated the average difference between the observed and the fitted T_e([O III]) of
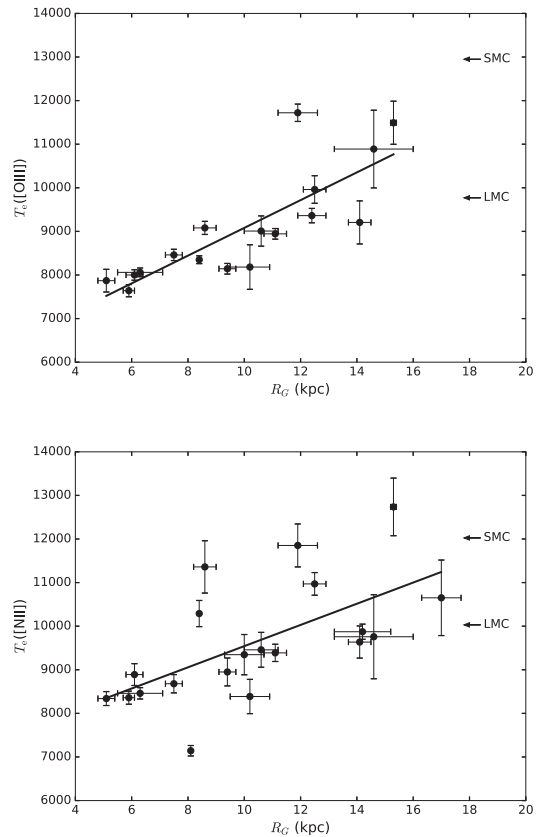

Figure A1. The radial distribution of the T_e([O III]) (upper panel) and T_e([N II]) (lower panel) for the whole sample of the Galactic H II regions (see the text for description of samples). The solid black line represents a least-squares linear fit to all objects. The arrows indicate the average T_e([O III]) and T_e([N II]) of the H II regions in the LMC and SMC (Domínguez-Guzmán et al. 2017; Toribio San Cipriano et al. 2017).

the H II regions by removing the outlier (Sh 2-298) and we obtained 430 K, a value closer to a mean observational uncertainty of 300 K.

Fig. A1 shows, for the first time, that the T_e([N II]) of H II regions in the Milky Way also varies with the galactocentric distance. The slope in the T_e([N II]), 240 ± 40 K kpc^{-1}, is somewhat lower than that obtained for the T_e([O III]) although the scatter is considerably larger. The mean difference between the observed and the fitted T_e([N II]) of the H II regions presented in Fig. A1 is 810 K, higher than the average uncertainty (390 K) of all T_e([N II]) determinations. The exact origin of this scatter is difficult to explain. N$^+$ is usually located in the outer regions of the nebulae, and depending on the relative development of the Strömgren spheres of the high and low ionization species, the differences between T_e([N II]) and T_e([O III]) may vary among different objects. The maximum difference we find in the sample is 2160 K (Sh 2-298) and additional three objects show differences of about 2000 K: IC 5146, NGC 3603 and Sh 2-83. It is interesting to note that three out of these nebulae are ionized by stars with effective temperatures higher or lower than the usual T_{eff} of O-type stars. IC 5146 is ionized by a B0.5 V star and shows the lowest ionization degree amongst the whole sample. NGC 3603 is the only optically visible, giant H II region in the Milky Way and contains several WR and hot O3-4 stars (Drissen 1999). As aforementioned in this section, Sh 2-298 is ionized by a WR star and also shows a large difference in T_e([O III]). Excluding the four objects showing very large differences (≥ 2000 K) between the observed and the fitted T_e([N II]), the average difference in the rest
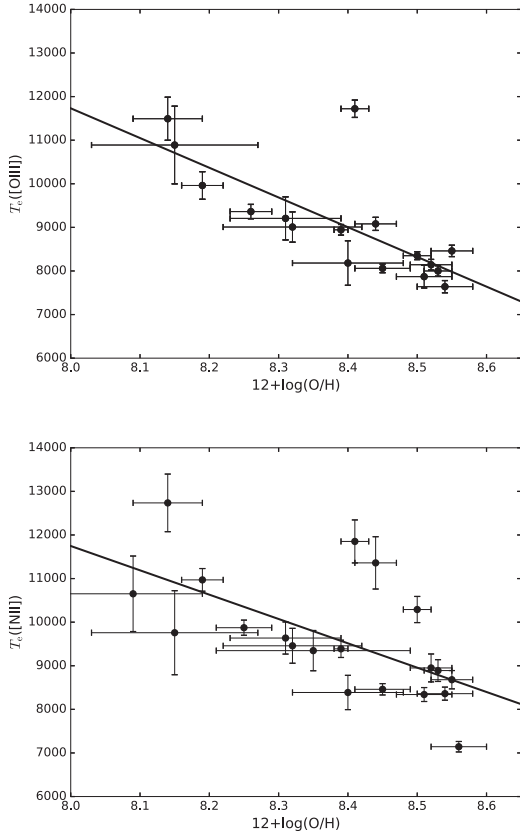
Figure A2. T_e([O III]) (upper panel) and T_e([N II]) (lower panel) versus O/H ratio for the whole sample of the Galactic H II regions. The solid black line represents a least-squares linear fit to all objects. The outlier in the upper panel corresponds to Sh 2-298, ionized by a WR star.
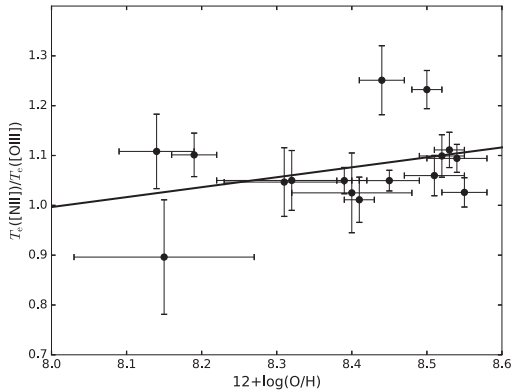

Figure A3. T_e([N II])/T_e([O III]) ratio versus O/H ratio for the whole sample of the Galactic H II regions. The solid black line represents a least-squares linear fit to all objects.

of the H II regions goes down to 520 K, much closer to the typical uncertainty of 390 K.

As we can see in Fig. A1, the expected values of T_e([O III]) and T_e([N II]) in H II regions in the outer disc of the Milky Way ($R_G \sim 17$ kpc) are, as in the case of the O/H ratios (see Fig. 7), between the mean values found for the H II regions in the LMC and SMC (Domínguez-Guzmán et al. 2017; Toribio San Cipriano et al. 2017). Remarkably, Fig. A1 does not give any hint about a flattening of the T_e gradient in the outer Galactic disc, reinforcing the conclusion drawn from Fig. 7.
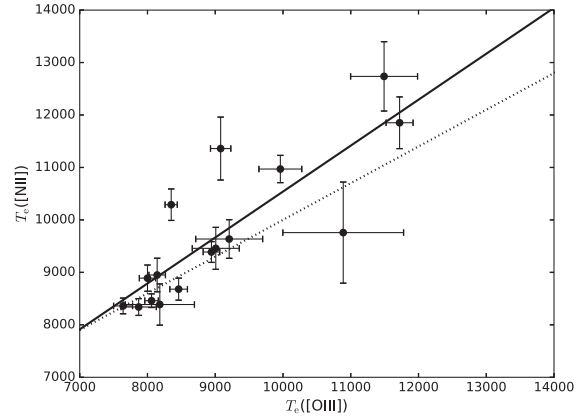
Figure A4. T_e([N II]) versus T_e([O III]) relation for the whole sample of the Galactic H II regions where both quantities have been determined. The solid black line represents a least-squares linear fit to all objects. The dotted line shows the classical relation from Garnett (1992) given in equation (A7).

In Fig. A2, we show the dependence of T_e([O III]) and T_e([N II]) with respect to the O/H ratio. In particular, the correlation between T_e([O III]) and the O abundance is specially tight. As expected, the objects showing the largest differences with respect to the linear fit are the same as in Fig. A1.

The least-squares linear fit to the T_e([O III]) versus O/H ratio relation gives

$$T_e([\text{O III}]) = -15540(\pm 3800)\text{K} - 6820(\pm 1070) \times \log(\text{O/H}) \tag{A3}$$

and to the T_e([N II]) versus O/H ratio relation gives

$$T_e([\text{N II}]) = -10580(\pm 4150)\text{K} - 5580(\pm 1160) \times \log(\text{O/H}). \tag{A4}$$

In Fig. A3, we show the dependence of the T_e([N II])/T_e([O III]) ratio with respect to the O abundance. The least-squares linear fit of the data included in that figure gives

$$T_e([\text{N II}])/T_e([\text{O III}]) = 1.80(\pm 0.48) + 0.20(\pm 0.13) \times \log(\text{O/H}), \tag{A5}$$

which indicates a very small or almost absent correlation between both quantities.

Finally, we have obtained the relation between T_e([N II]) and T_e([O III]) in Fig. A4, finding a relatively tight correlation and the following least-squares linear fit:

$$T_e([\text{N II}]) = 1780(\pm 1280)\text{K} + 0.88(\pm 0.15) \times T_e([\text{O III}]); \tag{A6}$$

the slope of the fit is consistent with a 1:1 relation considering the uncertainties. This fit is also very similar to the classical one obtained by Garnett (1992) using photoionization models and assuming T_e([N II]) = T_e([O II]):

$$T_e([\text{N II}]) = T_e([\text{O II}]) = 3000\text{K} + 0.7 \times T_e([\text{O III}]). \tag{A7}$$

Our T_e([N II])-T_e([O III]) relation is also consistent with that obtained by Esteban et al. (2009) from deep spectra for a sample of Galactic and extragalactic H II regions and Vale Asari et al. (2016) from the results of an extensive grid of modern photoionization models (see their fig. A2).